Ocean Modelling 176 (2022) 102071

Contents lists available at ScienceDirect

Ocean Modelling

journal homepage: www.elsevier.com/locate/ocemod

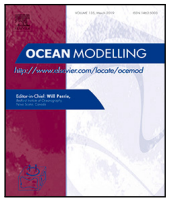

Resolving regions known for intense wave–current interaction using spectral wave models: A case study in the energetic flow fields of Northern Norway

Trygve Halsne [a,b,*], Patrik Bohlinger [a], Kai Håkon Christensen [a,c], Ana Carrasco [a], Øyvind Breivik [a,b]

[a] Norwegian Meteorological Institute, Henrik Mohns Plass 1, Oslo, 0371, Norway
[b] University of Bergen, Allégaten 41, Bergen, 5020, Norway
[c] University of Oslo, Problemveien 7, Oslo, 0315, Norway

ARTICLE INFO

Keywords:
Wave–current interaction
Tidal dynamics
Wave trapping
Water waves

ABSTRACT

Oceanic current forcing in spectral wave models have recently been demonstrated to have a large impact on wave heights at scales between one and up to several hundred kilometers. Here we investigate the impact of such forcing on open-ocean wave heights in Northern Norway using a high-resolution spectral wave model with currents from an ocean circulation model of similar resolution. We find that the wave model, to a large extent, resolves regions identified in the Norwegian Pilot Guide for maritime navigation as having dangerous sea states due to wave–current interaction. This is in contrast to a wave model forced with surface wind fields only. We present a novel diagnostic method to map the spatio-temporal scales associated with the wave height modulation between the two wave model predictions. The method is employed to map areas where significant wave–current interaction can be expected. In many cases, we are also able to confirm the physical mechanisms reported in the Pilot Guide, which are leading to an increase in wave energy due to currents. The largest wave height differences between the two models occur when waves and currents are opposing each other. In such situations, refraction and wave blocking are the dominating effects for the swell and wind sea parts of the spectrum, respectively. Furthermore, including current forcing significantly improves the agreement with in situ observations in strong tidal currents. Here, we see an increase in significant wave height of up to 50%. Even larger relative differences, exceeding 100%, are found in sheltered areas, with one specific region showing a reduction in model errors of 18% due to refraction and advection of wave action.

1. Introduction

Inclusion of ocean currents as forcing in spectral wave models is an active field of research, since it is one of the least developed and least verified parts in such models (Babanin et al., 2017, 2019). This is obviously important for day-to-day wave forecasting in regions with strong currents, but also for other aspects like modeling air–sea interactions due to the exchange of properties through the interface, which is key for climate predictions (Cavaleri et al., 2012). Ocean currents can modulate wave heights significantly, and even dominate the variability in the open ocean at scales of 10–100 km (Ardhuin et al., 2017). For shorter scales, sub-mesoscale fronts have been found to increase significant wave heights up to 30% (Romero et al., 2017), and twin model experiments have revealed wave height modulations up to 80% due to current-induced refraction in low wind conditions (Romero et al., 2020). Furthermore, periodic interactions in tidal currents is known to induce intense local wave height modulations, such as reported by Masson (1996).

Northern Norway is known for its extraordinarily strong open-ocean tidal currents (Gjevik et al., 1997). In addition, the region is subject to a turbulent flow field with strong eddies in the Norwegian Atlantic Current (NAC) and the Norwegian Coastal Current (NCC) (Mork, 1981), see Figs. 1, 2. Further to this, the northeast Atlantic is home to the most extreme wave climate globally (Aarnes et al., 2012). This makes Northern Norway an interesting region to study wave–current interaction as there is a steady influx of swell in addition to local windsea. Specific areas are known for intense interactions, described in detail in The Norwegian Pilot Guide (Den norske los, 2018, hereinafter NPG). Some are also mentioned in the classical literature (Gjevik et al., 1997). In the NPG, they are referred to as "areas of dangerous waves" (Fig. 3). This information was collected from an extensive survey among experienced sailors and local fishermen. In addition to mapping these areas, the survey also addressed the characteristic current and wave conditions presumed responsible for the choppy, and sometimes dangerous, sea states. However, there have been no attempts to resolve these areas

* Corresponding author at: Norwegian Meteorological Institute, Henrik Mohns Plass 1, Oslo, 0371, Norway.
Trygve Halsne (T. Halsne).
E-mail addresses: trygve.halsne@met.no (T. Halsne), patrikb@met.no (P. Bohlinger).

https://doi.org/10.1016/j.ocemod.2022.102071
Received 14 April 2022; Received in revised form 11 June 2022; Accepted 7 July 2022
Available online 14 July 2022

using spectral wave models. In this work, we aim to map areas known (or not known) for high and dangerous sea states presumed due to wave–current interaction using state-of-the-art wave and ocean models. Moreover, as different flow regimes (e.g., tidal and sub-mesoscale) are associated with various temporal and horizontal scales, we investigate if such a model coupling also resolves spatio-temporal variability in the wave field, including the extreme values in specific regions like strong tidal currents.

Only a few studies have investigated the impact of currents on the wave field in Northern Norway. Segtnan (2014) used the wave refraction model by Mathiesen (1987) and found that the wave propagation direction close to the coast was often misaligned with the wave direction offshore. The misalignment was attributed to current-induced refraction due to the eddies associated with the NCC. Saetra et al. (2021, hereinafter OS21) investigated wave–current interaction in the Lofoten Maelstrom, which is one of the world's strongest open-ocean tidal currents. They found that wave breaking increased during maximum current speeds. This was associated with an increase in wave height due to horizontal gradients in the tidal current. Neither of these studies sufficiently examined the flow fields impact on the wave height, and the associated horizontal variability.

Here we investigate the impact of currents by comparing the results from a twin experiment with identical spectral wave models (hereinafter wave models) with different forcing, i.e., one with wind and currents and one forced with wind only. Similar model setups have recently been shown to yield acceptable results on large (e.g. Marechal and Ardhuin, 2021), intermediate (e.g. Kanarik et al., 2021) and small horizontal scales (e.g. Romero et al., 2020), including tidal currents (Ardhuin et al., 2012). We assess the impact by different current regimes on the wave field by analyzing specific events and by comparing them with in situ and remote sensing observations. We also present a novel, generic, method to map spatio-temporal variability in twin experiments based on time series analysis, which in this context is used to map regions with strong wave–current interaction. More generally, we assess the usefulness of such an approach for sensitivity analysis in twin model experiments.

The paper is structured as follows: In Section 2, we provide a description of the models, forcing, and observations together with metrics and methods used for validation. In Section 3, we present our results, which are further discussed in Section 4. We then present our concluding remarks in Section 5.

2. Materials and methods

2.1. Models and observations

2.1.1. Model domain and study period

The model domain covers the coast of Northern Norway (Fig. 1), an area with extensive maritime activity, including ship traffic, fisheries, marine engineering, and marine harvesting (fish farming). The domain is identical to the high resolution operational wave forecast model at the Norwegian Meteorological Institute for this region. Northern Norway is located in the belt of westerlies and is thus dominated by westerly winds and waves. Specific areas in the region are subject to vigorous tidal currents due to the semi-diurnal northward propagating Kelvin wave. One of these is the aforementioned Lofoten Maelstrom located on the southern tip of *Lofoten* (location 7—Fig. 1 local names are referred to in italic). The tidal current's local name is *Moskstraumen*, which we will use here (see B—Fig. 1). Combined with the Norwegian Coastal Current that meanders northward, loosely following the bathymetry of the shelf, these strong tidal currents give rise to very strong current gradients.

This study covers the period from 2018-12-01 until 2019-02-28, which includes six spring tide periods and some storms mainly approaching the continental shelf from the west outside *Lofoten*. Six times during the period, H_s reached values above 6 m (not shown). The particular period was chosen since it overlaps with in situ observations from a measurement campaign in *Moskstraumen* (Saetra et al., 2021). We pay particular attention to the locations denoted A and B and those numbered 2–8 in Fig. 1. The first (A and B) denote the location of the in situ observations while the latter (2–8) denote areas known for dangerous waves according to their numbering in the NPG (see Fig. 3). The reason why we start counting on 2, is that area 1 is outside our model domain.

2.1.2. The WAM spectral wave model

We used a recent version of the wave model WAM, Cycle 4.7 (Komen et al., 1994; Behrens et al., 2013). WAM solves the wave action balance equation

$$\frac{\partial N}{\partial t} + \frac{1}{\cos(\phi)}\frac{\partial}{\partial \phi}\left(\dot{\phi}\cos(\phi)N\right) + \frac{\partial}{\partial \lambda}\left(\dot{\lambda}N\right) + \frac{\partial}{\partial \omega}\left(\dot{\omega}N\right) + \frac{\partial}{\partial \theta}\left(\dot{\theta}N\right) = \left(S_{\text{in}} + S_{\text{nl}} + S_{\text{ds}} + S_{\text{bot}}\right)\sigma^{-1}, \tag{1}$$

where $N = E/\sigma$, the wave action density, is the ratio of the spectral wave energy density, $E = E(t, \phi, \lambda, \omega, \theta)$, and the intrinsic wave angular frequency, σ. Furthermore, t, ϕ, λ, ω, and θ denote time, latitude, longitude, angular frequency, and direction, respectively. The right hand side in (1) denotes the parameterized physical processes which represents the wind input (S_{in} from Ardhuin et al., 2010), non-linear wave–wave interactions (S_{nl} from Hasselmann et al., 1985), wave dissipation due to white capping (S_{ds} from Ardhuin et al., 2010), and bottom friction (S_{bot} from Hasselmann et al., 1985). The terms denoted with overdots in Eq. (1) describe the wave kinematics governed by

$$\dot{\phi} = \left(c_g\cos(\theta) - U\right)R^{-1}, \tag{2}$$

$$\dot{\lambda} = \left(c_g\sin(\theta) - V\right)\left(R\cos(\theta)\right)^{-1}, \tag{3}$$

$$\dot{\omega} = \frac{\partial \Omega}{\partial t}, \tag{4}$$

$$\dot{\theta} = c_g\sin(\theta)\tan(\phi)R^{-1} + \dot{\theta}_D, \tag{5}$$

where $\mathbf{U} = (U, V)$ is the horizontal surface current velocity vector, R is the radius of the earth, c_g is the wave group velocity, and

$$\dot{\theta}_D = \left(\sin(\theta)\frac{\partial}{\partial \phi}\Omega - \frac{\cos(\theta)}{\cos(\phi)}\frac{\partial}{\partial \lambda}\Omega\right)(kR)^{-1}. \tag{6}$$

Here, $\mathbf{k}$ is the wave number vector and $k = |\mathbf{k}|$. Latitudinal and longitudinal advection of wave action by the wave group velocity and the ambient current are represented by Eqs (2)–(3). The temporal change of angular frequency is given by Eq. (4), where Ω is the Doppler-shift dispersion relation

$$\omega = \Omega(\mathbf{k}, \mathbf{x}, t) = \sigma + \mathbf{k}\cdot\mathbf{U}, \tag{7}$$

where $\mathbf{x} = (x, y)$ is the horizontal positional vector. The intrinsic frequency follows the linear dispersion relation

$$\sigma = \sqrt{gk\tanh(kd)}. \tag{8}$$

Here g, d are the gravitational acceleration and water depth, respectively. The refraction, or turning, of waves due to gradients in the ambient current and bathymetry is dictated by Eq. (5).

The model was set up on a regular grid with 800 m horizontal grid resolution. It had a spectral resolution of 24 directional and 30 frequency bins, ranging from $f_0 = 0.034523$ Hz to $f_{29} = 0.5476419$ Hz in logarithmic increments such that $f_i = f_0 \times 1.1^i$ where $i = 1, 2, \ldots, 29$. Model integration time steps of 30 s were used for both the propagation and source term computations. For the boundaries, we used hourly 2D spectra from the European Centre for Medium-Range Weather Forecasts (ECMWF).

We performed a twin model experiment using the same model specifications and physical parameterizations. Both were forced with surface winds, but one also included current forcing. These two runs are hereinafter referred to as the reference run, $\text{WAM}_{\mathbf{ref}}$, i.e., with zero currents, and the run including currents, $\text{WAM}_{\mathbf{curr}}$. The current forcing is not part of the source term calculations but is included in the wave kinematics [the left hand side of Eq. (1)], as shown in Eqs. (2)–(5).

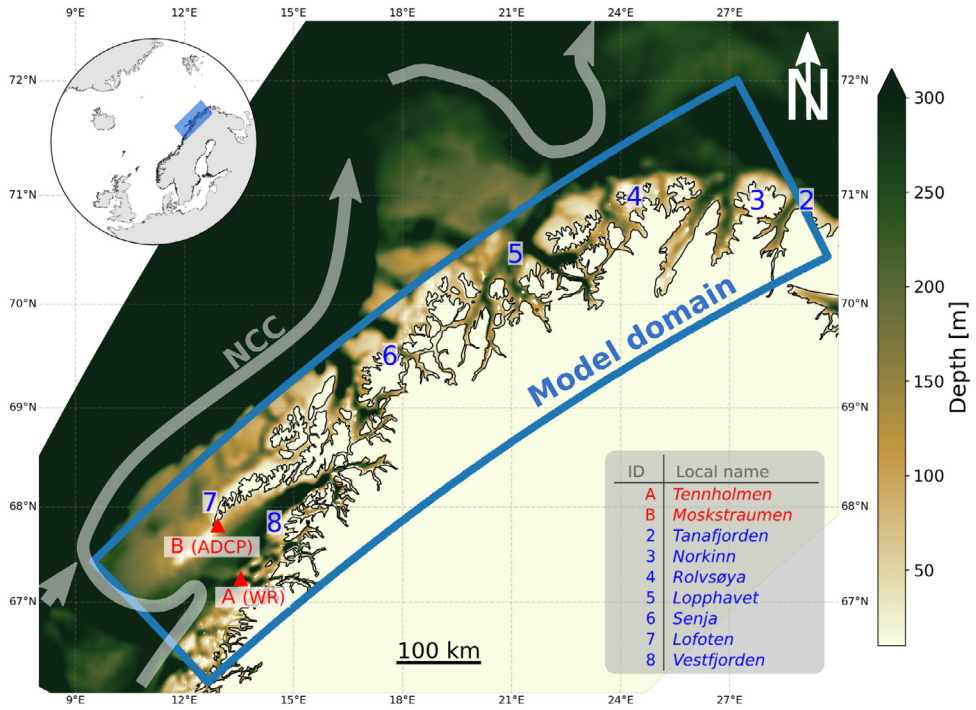

Fig. 1. The study area along the coast of Northern Norway. The Norwegian Atlantic Current (not shown) and the Norwegian coastal current (NCC) are the main ocean currents in the region, the latter guided northwards by the bathymetry. The WAM spectral wave model domain is outlined by the blue curvilinear polygon. Within the domain, two in situ measurement devices provided observations during the study period. These are the wave rider (WR) buoy outside A–*Tennholmen* and the ADCP located in the tidal current B–*Moskstraumen*. Additional local reference points are listed in the legend.

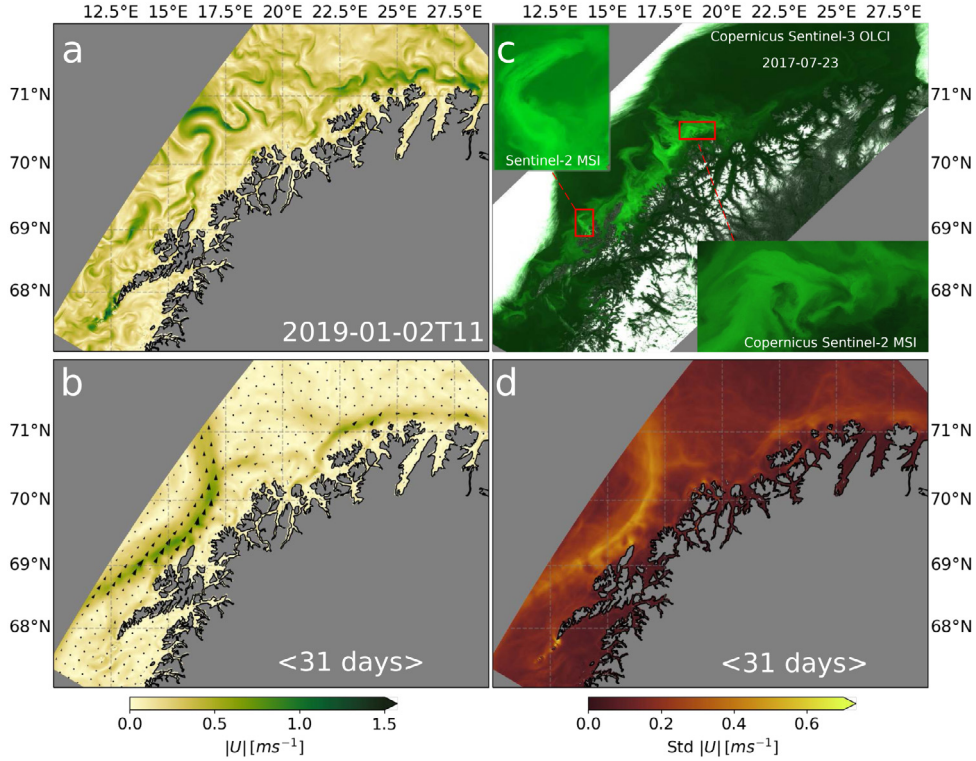

Fig. 2. A view of the Norkyst 800 m ROMS ocean model is given in panels (a), (b), and (d). Panel (c) illustrates the small scale variations of the Norwegian Coastal Current (NCC) during an algal bloom captured by the optical Copernicus Sentinel-2 and Sentinel-3 missions in 2017. The surface current speed, |U|, average speed, and standard deviation, are shown in panels (a), (b), and (d), respectively. Panel (a) show a snapshot of the ocean model surface current speed. The surface current mean flow (with directions) and the current variability (in terms of its standard deviation) are shown in panels (b) and (d), respectively. Here, the current statistics are computed for all days in January 2019.

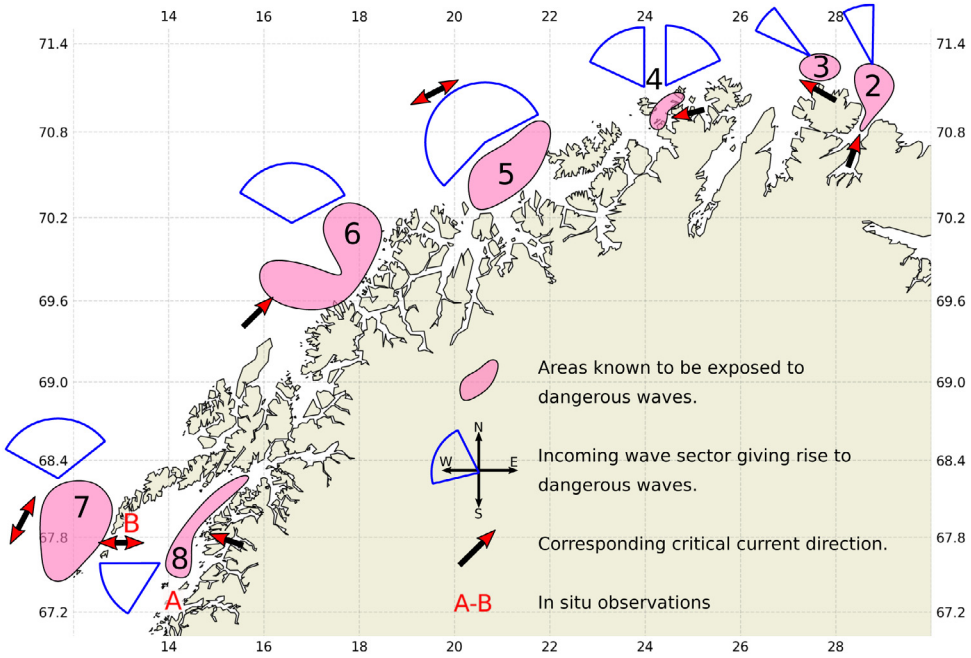

Fig. 3. An overview of the areas known for dangerous waves, according to the Norwegian Pilot Guide (Den norske los, 2018, NPG). Pink areas indicate the approximate horizontal extent of the critical areas (reproduced from the original publication), and their numbering is according to the original index. Area number 1 is outside the model domain and hence not included. Blue denotes the wave propagation sector associated with dangerous waves, and arrows denote the corresponding critical current direction.

2.1.3. Wave model forcing

NorKyst800 provided the ocean surface currents fields used to force $\mathrm{WAM_{curr}}$. This is an operational configuration of the Regional Ocean Modelling System (ROMS, see Shchepetkin and McWilliams, 2005) operated by the Norwegian Meteorological Institute. It is a three-dimensional ocean circulation model (hereinafter ocean model) with 800 m horizontal resolution and 42 vertical levels using topography-following coordinates. The ocean model is forced at the boundaries by the Hybrid Coordinate Ocean Model, which is part of the TOPAZ system operated for the pan-European Copernicus Marine Service (https://cmems.met.no/ARC-MFC/). Eight tidal constituents are included in the barotropic boundary conditions. Further specifications of the ocean model setup are given by Albretsen et al. (2011).

The ocean model gives a good representation of the currents along the coast of Norway, which is dominated by the NAC and the NCC, together with the tides (Christensen et al., 2018; Kristensen and Gusdal, 2021). The NCC on average flows northwards (Fig. 2b), and is loosely following the isobaths of the continental shelf (Fig. 1). Smaller-scale dynamics includes sub-mesoscale eddies (i.e., of the order of 0.1–10 km, see McWilliams, 2016) originating from baroclinic instabilities (Fig. 2a), and inertial currents resulting from the wind forcing (Röhrs and Christensen, 2015). The appearance of eddies are readily observed indirectly by optical satellite instruments if algal blooms are present (Fig. 2c). Their exact location in the ocean model is, however, associated with larger uncertainty compared with the mean flow. Baroclinic dynamics associated with the NCC are also transient, as they are advected northwards by the mean flow. The variability of the NCC is also strongly modulated by the tides (Fig. 2d). Further to this, several areas close to the shoreline have high variability but with a weak mean flow. This includes *Moskstraumen* where OS21 found the horizontal extent, magnitude, direction and phase of the modeled current field to be in reasonable agreement with in situ and satellite observations.

Wind forcing was taken from the operational forecasts generated by the Arome Arctic numerical weather prediction model operated by the Norwegian Meteorological Institute. It is a 2.5 km horizontal resolution non-hydrostatic model with 65 vertical levels, and is primarily based on the High Resolution Limited Area Model (HIRLAM)–ALADIN Research on Mesoscale Operational NWP in Euromed (HARMONIE) AROME configuration. Further specifications are given in Müller et al. (2017). We used the surface wind fields, $\mathbf{U}_{10}$, as input to S_{in}.

2.1.4. In situ observations

Observations from two instruments located in the southern part of the model domain were available during the period studied (see A,B Fig. 1). The first, a Nortek Signature 500 acoustic Doppler current profiler (ADCP), was located east in *Moskstraumen*. These measurements were reported by OS21, where a more complete description of the data set and the area can be found. The observations include standard integrated wave parameters like significant wave height and the mean wave period, together with wave directional information. In addition, the ADCP measured the vertical profile of the current, which is barotropic during the tidal cycles (OS21). Wave measurements during two of the spring tide events were sometimes flagged as invalid at maximum current speed because the instrument tilted beyond the operating range (10° from zenith).

The second in situ instrument is a Datawell Mk3 waverider buoy (WR), moored near the island of *Tennholmen*. This buoy reported significant wave height and mean zero upcrossing period T_z with hourly temporal resolution.

For practical purposes, we denote both the observed and spectral estimate of significant wave height as H_s since they are very similar (Holthuijsen, 2007). The same applies for the mean wave period, hereafter denoted T_{m02}.

The maximum observed H_s values were about 8.5 m and 10.5 m from the ADCP and the WR, respectively (not shown).

2.1.5. Remote sensing observations

Several satellite altimeter missions are archived and openly accessible through the ESA Sea State Climate Change Initiative (CCI, https://data.ceda.ac.uk/neodc/esacci/sea_state/data/v1.1_release/l2p) and the Copernicus Marine Service (https://marine.copernicus.eu/). This includes the Copernicus Sentinel-3 missions together with the SARAL/AltiKa and Cryosat −2. It is common to filter and resample Level-2 20 Hz (approx. 350 m resolution) retrievals to Level-3 1 Hz (approx. 7 km resolution) (Bohlinger et al., 2019). For December 2018, we used the Level-3 multimission dataset from CCI. For January

and February 2019, we used the Sentinel-3 Level-3 data since the multi-mission dataset does not yet cover this period.

2.2. Verification

2.2.1. Verification metrics

For verification against observations, we computed the normalized root mean squared error (NRMSE) and normalized bias (NBIAS) using the same definition as that of Ardhuin et al. (2010),

$$\mathrm{NRMSE}(X) = \sqrt{\frac{\sum(X_\mathrm{o} - X_\mathrm{m})^2}{\sum X_\mathrm{o}^2}}, \tag{9}$$

$$\mathrm{NBIAS}(X) = \frac{\sum(X_\mathrm{o} - X_\mathrm{m})}{\sum X_\mathrm{o}}. \tag{10}$$

Here subscripts "o" and "m" denote observation and model, respectively, and X denotes the variable. For model intercomparison, we denote the absolute difference between the two wave model integrations as $\Delta X = \mathrm{WAM}_{\mathbf{curr}} - \mathrm{WAM}_{\mathbf{ref}}$. Relative changes between the model runs are denoted as

$$\mathrm{RC}(X) = \frac{\Delta X}{X_\mathrm{ref}}, \tag{11}$$

where the subscript "ref" indicates values from $\mathrm{WAM}_{\mathbf{ref}}$. Instead of the NRMSE, we computed the RMSE in this respect. Further, we computed the mean, standard deviation (σ) and minimum/maximum difference.

2.2.2. Spatio-temporal variability

Since the ocean circulation within the model domain is dominated by the NCC, inertial currents, and the tides, we expect wave heights to be modulated on the associated temporal scales. For tides we consider the M_2 semidiurnal tidal constituent. The inertial frequency is the about the same as M_2 in the area, making it difficult to discriminate these in the open ocean. Close to shore, however, the topography cancels the inertial response. For baroclinic instabilities associated with the NCC, namely, fronts and eddies, we consider frequencies between hours to a couple of days, which generally reflect their life cycle (McWilliams, 2016). In order to separate the dominant temporal modes and their associated energy, we conducted a time series analysis for all grid points in our model domain, similar to the single point analysis by Gemmrich and Garrett (2012) and OS21. That is, power spectral densities (PSDs) for each model grid point, (i, j) were computed for a specific difference variable ΔX (i.e. $\mathrm{WAM}_{\mathbf{curr}} - \mathrm{WAM}_{\mathbf{ref}}$). We now compute the energy associated with the low-frequency band $[f_0, f_1]$, namely the NCC (denoted by index 1), and the high-frequency band $[f_2, f_3]$, namely M_2 (denoted by index 2), as

$$\hat{E}_{1,(i,j)} = \int_{f_0}^{f_1} \mathrm{PSD}(\Delta X)_{(i,j)}\, df, \tag{12}$$

$$\hat{E}_{2,(i,j)} = \int_{f_2}^{f_3} \mathrm{PSD}(\Delta X)_{(i,j)}\, df. \tag{13}$$

For convenience we here consider H_s since it is proportional to the square root of the wave energy. Note that $\hat{E}$ represents the variance of ΔX summed over a specific frequency range and should not be confused with the wave energy density E.

To help visualize the variability of the two frequency bands, we now create a red–green–blue (RGB) color composite showing the spatio-temporal variability of $\hat{E}$ as (R,G,B) = ($\hat{E}_1$, $\hat{E}_2$, $\hat{E}_1$). Variations associated with the low frequencies (1) appear as purple (equal amounts of red and blue), while variations associated with high frequencies (2) appear as green. Black then comes to represent zero variability while white means both temporal scales are present in equal amounts. This is a method which is frequently used in remote sensing applications for multitemporal change detection analysis (e.g. Marin et al., 2015), but to our knowledge has not been applied to spatial spectral analysis of wave model fields before.

Table 1
Bulk validation metrics for H_s and T_{m02} computed for the wave models vs. observations.

	NBIAS		NRMSE	
	$\mathrm{WAM}_{\mathbf{curr}}$	$\mathrm{WAM}_{\mathbf{ref}}$	$\mathrm{WAM}_{\mathbf{curr}}$	$\mathrm{WAM}_{\mathbf{ref}}$
H_s				
ADCP (N = 3767)	0.119	0.120	0.215	0.216
WR (N = 2133)	0.109	0.100	0.181	0.174
Altimeter (N = 1913)	0.05	0.05	0.21	0.21
T_{m02}				
ADCP (N = 3500)	0.185	0.194	0.170	0.175
WR (N = 2133)	0.134	0.115	0.181	0.174

3. Results

3.1. Wave model validation against observations

3.1.1. In situ observations and bulk validation

Energy fluctuations at each observation location are investigated through a power spectral density (PSD) analysis of ΔH_s (Fig. 4a) and H_s observations (Fig. 4b). For $\mathrm{WAM}_{\mathbf{curr}}$ in *Moskstraumen*, the most distinct frequency peaks are located around the tidal constituents M_2 and M_4 as well as near the inertial frequency, f, which is about the same as M_2 in the area (Fig. 4a). This is in accordance with the observations, with pronounced peaks around M_2 and M_4 (Fig. 4b), where the latter is shifted slightly toward lower frequencies in $\mathrm{WAM}_{\mathbf{curr}}$. At *Tennholmen*, the M_2 signal in ΔH_s is about two orders of magnitude smaller than *Moskstraumen*, which makes sense since the area is not exposed to strong tidal currents (Fig. 4).

For frequencies below M_2, the underlying causes for the inter-model discrepancies are many (Fig. 4a). Firstly, there is a delayed response in the mean flow due to the synoptic weather systems. OS21 found wave breaking in *Moskstraumen* to correspond well with the passage of such systems for frequencies below 0.75 cycles per day (see their Fig. 4c). Secondly, the refraction of wave action density due to eddies and whirls affects the wave height variability on longer time scales than those of the tides. This will be discussed in detail later. Thirdly, during one of the storms within our study period (e.g. $H_\mathrm{s} > 6$ m), ΔH_s exceeded 2 m in *Moskstraumen*. Thus, strong wave height modulations occurred infrequently. Such a storm event is further elaborated in Appendix.

In terms of verification metrics, the overall performance of the wave model compared against the observations is listed in Table 1. Both model runs have a negative bias of about 10% in H_s compared with the in situ observations. The NRMSEs are in the range 17–22%, and inter-model differences are below 1%. We find slightly higher differences in NBIAS and NRMSE for T_{m02} (Table 1). This is similar to the results of Palmer and Saulter (2016), who also reported inconclusive bulk validation metrics but found a more realistic representation of the wave field sub-regions dominated by tides. Model errors accumulate in such metrics if the spatio-temporal variations between model output and observations are slightly out of phase. Due to this, Ardhuin et al. (2012) found increasing wave model errors in tidal currents against a wave model forced with wind only.

3.1.2. Altimeter observations

When considering the entire domain, the NBIAS and NRSME against altimeter observations of H_s are virtually identical for both model runs (Table 1). However, sub-regions expected to have significant wave–current interaction (Fig. 5) do reveal a systematic improvement for all validation parameters for $\mathrm{WAM}_{\mathbf{ref}}$ in *Vestfjorden* (location 8 in Fig. 1) with a 16% reduction in bias in December 2018 (P5, Table 2). Albeit a bit less, a decrease in model error and bias can also be seen for P5 from the CMEMS product. Here, there are twice as many samples as in December 2018 (N = 76 vs N = 29).

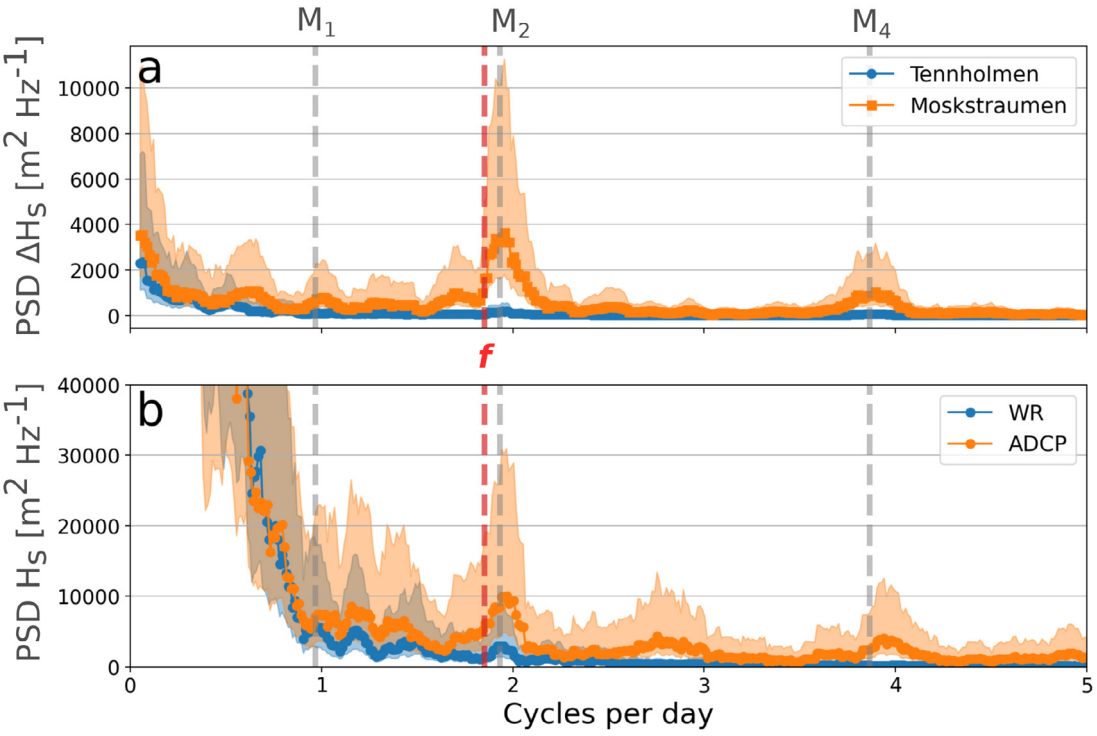

Fig. 4. Power spectral density (PSD) plots of ΔH_s (= WAM_{curr} - WAM_{ref}) and H_s time series at the in situ observation locations covering the study period. Panel (a) shows ΔH_s from grid points closest to the ADCP and wave rider (WR) locations. Panel (b) shows PSDs computed for the H_s observations in *Moskstraumen* (ADCP) and *Tennholmen* (WR). The shaded region around the PSDs indicates the 95% confidence limits. The tidal constituents M_1, M_2, and M_4 are plotted as vertical gray dashed lines for reference together with the inertial frequency, f (red dashed line).

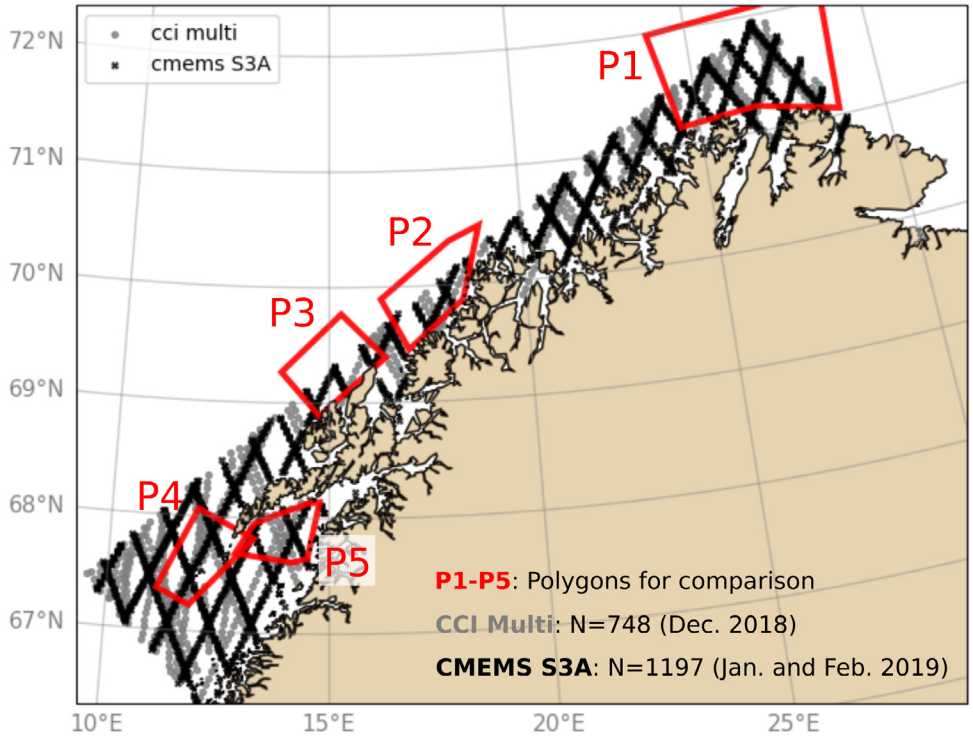

Fig. 5. Altimeter level-3 H_s observations within the model domain from the CCI multimission (gray) and CMEMS (black), together with polygons (P1–P5) for regional comparison.

3.2. Large-scale model inter-comparison

3.2.1. Temporal modes in horizontal H_s variability

In addition to the lowest frequencies (see Section 3.1.1), we find that ΔH_s exhibits two main temporal scales, controlled by the baroclinic instabilities associated with the NCC (T_e) and the M_2 semidiurnal tidal constituent (T_t). In general, the life-cycle of eddies and fronts lasts from hours to days depending on their generating mechanism and the prevailing conditions (McWilliams, 2016). In our domain we find that normally $T_e > T_t$ (not shown). Since the wind forcing is the same in

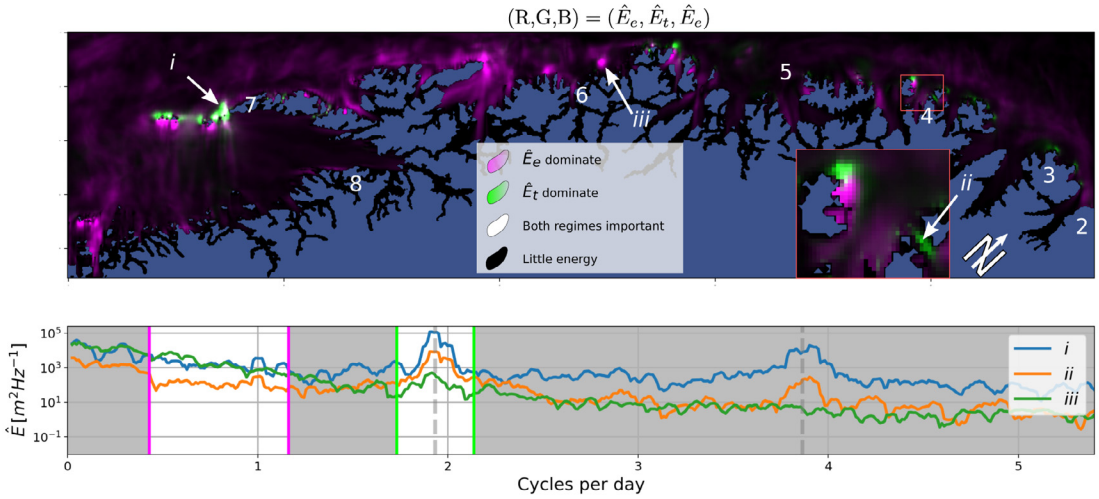

Fig. 6. Characterization of spatio-temporal variability in ΔH_s. The image consists of $\hat{E}_e$, $\hat{E}_t$, and $\hat{E}_c$ from Eqs (14)–(15) on the R, G, and B channels, respectively. Hence, shadings of purple signify areas where the variability is associated with $\hat{E}_e$ while shadings of green correspond to $\hat{E}_t$. White (black) show areas where both (none) of the modes have energy. The PSDs originate from a time series analysis for each model grid point. A few selected cases are shown in the lower panel for *Moskstraumen* (label *i*), *Breisundet* (label *ii*), and *Senja* (label *iii*). The gray shaded areas denote the frequencies that are excluded in the analysis, and the vertical dashed lines denote the M_2 and M_4 tidal constituents. Numbering 2–8 denote the dangerous wave areas from Fig. 3.

Table 2
Validation metrics computed for specific sub-regions (polygons P1–P5 in Fig. 5) against altimeter observations of H_s. Pearson correlation coefficient is denoted *r*.

	NBIAS		NRMSE		r	
	WAM_{curr}	WAM_{ref}	WAM_{curr}	WAM_{ref}	WAM_{curr}	WAM_{ref}
December 2018 CCI multimission						
P1 (N = 62)	0.18	0.17	0.21	0.21	0.91	0.91
P2 (N = 21)	0.00	−0.02	0.17	0.15	0.64	0.70
P3 (N = 37)	0.12	0.12	0.18	0.18	0.92	0.92
P4 (N = 165)	−0.01	−0.01	0.12	0.13	0.93	0.92
P5 (N = 29)	0.47	0.63	0.53	0.71	0.40	0.25
January–February 2019 CMEMS						
P1 (N = 88)	0.05	0.04	0.20	0.18	0.87	0.89
P2 (N = 93)	−0.04	−0.04	0.19	0.19	0.94	0.94
P3 (N = 106)	−0.01	−0.01	0.27	0.26	0.71	0.73
P4 (N = 344)	0.10	0.10	0.24	0.24	0.89	0.90
P5 (N = 76)	0.26	0.32	0.33	0.37	0.91	0.90

WAM_{curr} and WAM_{ref}, T_e and T_t should be resolved by WAM_{curr} only. We used Eqs (12)–(13) to discriminate these temporal modes as follows,

$$\hat{E}_{e,(i,j)} = \int_{\delta f_0}^{M_1+\delta f} \mathrm{PSD}(\Delta H_s)_{(i,j)}\, df, \tag{14}$$

$$\hat{E}_{t,(i,j)} = \int_{M_2-\delta f}^{M_2+\delta f} \mathrm{PSD}(\Delta H_s)_{(i,j)}\, df. \tag{15}$$

Here, δf_0 correspond to about 0.4 cycles per day and constitute a low pass filter, and δf correspond to about 3 h.

An RGB composite showing the spatio-temporal variability of ΔH_s is given in Fig. 6. It is clear that the tides impact the wave height in the area surrounding *Lofoten*, in particular in *Moskstraumen* (*i*,7 Fig. 6). Here, the energy modulation at M_2 is an order of magnitude larger compared with other areas dominated by tidal currents (lines *i* and *ii* Fig. 6). Furthermore, tidal processes mostly dominate close to the coast, including in narrow sounds and channels. In addition to bathymetric effects, some of these are also affected by corner effects that locally accelerate the tidal current. We also performed an analysis including the M_4 components, which gave more or less the same result (not shown).

In some regions, T_e and T_t appear simultaneously, but spatially separated, as in the highlighted box. In these cases, the wave height modulation is most often associated with the tides, but $\hat{E}(M_2)$ can be orders of magnitudes lower than $\hat{E}(M_1)$ (not shown). Thus, the wave–current interaction is dominated by tidal processes, but local topographic conditions like the corner effect can affect the flow field, and also and the incoming wave field. For the latter, refraction is very sensitive to the incoming wave direction, and waves can at times be refracted into sheltered areas.

Between areas 6 and 7, modulation on T_e is most pronounced (Fig. 6). Here, some places have a strong M_1 signal, while others are modulated on longer time scales, similar to the shallow banks outside *Senja* (see *iii*,6 Fig. 6).

Further away from the coast, T_e is more pronounced, but with less variability, as seen south and west of *Lofoten* (7– Fig. 6). This also includes the strip north of *Rolvsøya* (location 4– Figs. 1,6), where the NCC is meandering with strong eddy activity and large current variability (Figs. 2a,d). As expected, this suggests that wave refraction due to eddies and whirls is what drives the differences between the two wave model runs in such areas. Furthermore, it shows that wave–current interaction becomes more intense in areas close to the coast with strong tides than further away from the coast.

3.2.2. Statistical variability

There are some systematic differences in the twin model experiment. An area which stands out is *Vestfjorden* (8– Fig. 1), where on average $\Delta H_s > 0$ (i.e., $WAM_{curr} > WAM_{ref}$ in Fig. 7a). The region stands out even more clearly in terms of the relative change (RC), with mean ΔH_s values from +20% and above, and maximum values well above 100% (Figs. 8a,c). For ΔT_{m02}, the mean value in *Vestfjorden* is between $0.5 - 1$ s with maxima around +3 s (not shown). Considering the Doppler shift and conservation of wave action, one would expect the increasing wave periods to be associated with decreasing wave amplitude. However, ΔH_s is positive, suggesting other dominating mechanisms (Figs. 7a, 8a).

Vestfjorden is sheltered from the strongest winds and has in general lower waves compared with the more exposed areas in the Lofoten archipelago. The systematic increase in H_s is mainly caused by advection of wave action due to the tidal oscillations and the NCC, together with current-induced refraction. To illustrate the impact of these effects, we inspect a case on 2019-01-05 shown in Fig. 9. Here, the area was dominated by eastward propagating swell and calm westerly winds and H_s about 0.1 m and 0.6 m in WAM_{ref} and WAM_{curr}, respectively (not shown). The wind sea wave height was more or less the same in both models (lower middle left panel of Fig. 9). The swell heights, however, were larger in WAM_{curr}, and the mean swell direction was

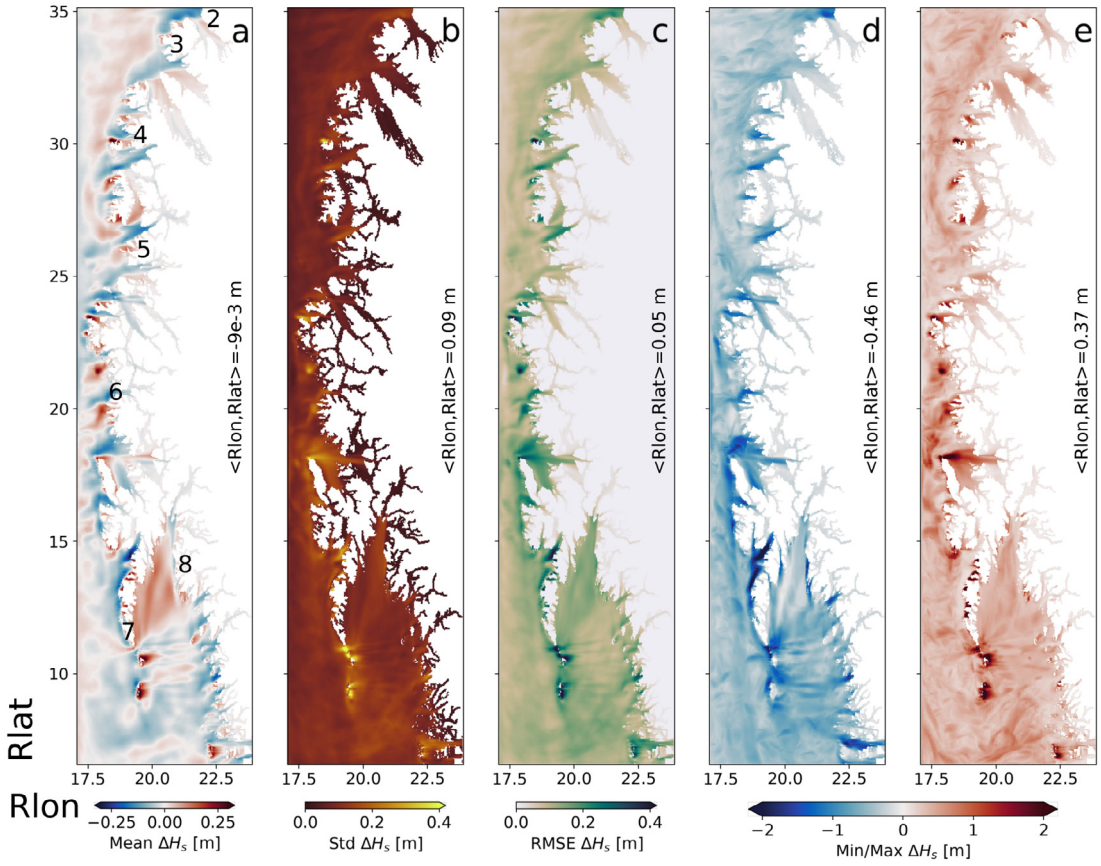

Fig. 7. Horizontal variability of ΔHs statistics including the mean (a), σ (b), RMSE (c) and minimum/maximum values [(d)/(e)]. All parameters are computed for the entire study period. The mean value for all grid points are denoted in each panel by "<Rlon, Rlat>". Minimum and maximum values denote the extremes for each grid cell and does not, necessarily, originate from the same time steps. Numbering 2–8 denote the dangerous wave areas from Fig. 3.

more northwards compared with WAM_{ref} (upper middle right panel of Fig. 9). Swell enters *Vestfjorden* through *Moskstraumen*, and meets strong current dipoles caused by the tidal current (see Fig. 9 OS21 and Fig. 8 Børve et al., 2021). Current-induced refraction is strongly connected to the vertical vorticity ζ of the current (Dysthe, 2001), and the dipoles thus have a strong influence on the wave propagation paths when propagating through *Moskstraumen*, as shown by OS21 (their Fig. 12). The influence of current refraction on swell can also explain the aforementioned mean increase in ΔT_{m02} with longer swell propagating into *Vestfjorden* in WAM_{curr} (upper right hand panel of Fig. 9). In addition to refraction in *Moskstraumen*, the advection of wave action from the south by the NCC (see Fig. 1) also modulates the wave field. The mean H_s difference for a 24 hour period was higher in WAM_{curr}, despite the changing vorticity field in *Moskstraumen* due to the tidal current (lower right panel of Fig. 9). The accumulation of wave action in *Vestfjorden* is in accordance with the results of Ardhuin et al. (2017), who found refraction and advection effects to dominate and partially cancel each other for scales larger than 30 km. Inclusion of current forcing tends to also reduce the horizontal difference in H_s across the *Lofoten* peninsula (not shown).

The shallow banks outside *Senja* reveal a positive mean and large maximum ΔH_s (location 6– Fig. 7). There are also several locations in lee of the mean NCC that exhibit substantial differences in wave energy connected to flow acceleration from corner effects (Fig. 7a). It is also interesting to note the separation between areas of positive and negative mean ΔH_s in the northernmost part of the model domain (e.g., between areas 3 and 4 in Fig. 7). Here, areas with on average positive ΔH_s are located away from the coast, i.e., collocated with regions of higher eddy activity and large current variability (Figs. 2a,d), and areas that are on average negative are located closer to the coast. The σ, RMSE, and min/max values indicate some hot spots mostly located close to the shoreline and associated with strong tidal currents (Fig. 7, panels b–e). These coincide with the strongest signal in the spatio-temporal analysis in Fig. 6.

3.3. Mapping regions with dangerous sea states

The regions identified by the NPG have been analyzed using the twin model experiment and observations (Fig. 3). We chose to investigate the areas where the ocean and wave models are expected to represent the dominating physical processes, and where the NPG gives a sufficient description of the phenomenon and underlying cause. Hence, area 2 is excluded in the analysis. In the subsequent sections, the regions are categorized according to their dominant cause. *Moskstraumen* (area 7) is highlighted because of the intense wave–current interactions as well as the availability of in situ observations.

3.3.1. Area 3 and 4: Opposing waves and tidal currents

Area 3 is exposed to the open ocean, as well as being subjected to a shallow plateau between 30–70 m (location 3 Fig. 1) which causes additional acceleration of the current. There is a clear tidal modulation of the wave field close to shore, where WAM_{curr} predicts higher mean wave height values (3– Figs. 6, 7a). The sharp transition to negative ΔH_s values further away from the coast is due to the mean flow direction of the NCC being eastward, together with waves primarily coming from west. In addition, the counter-flowing M_2 component is much weaker further out. Maximum increase in wave heights for this area was up to 40% in the period studied (Fig. 8c).

Although not confirmed with in situ measurements, the current in *Rolvsøysundet* and *Breisundet* (Rs and Bs in Fig. 10) is estimated to exceed 1 ms^{-1} (Den norske los, 2018). During spring tide, the current

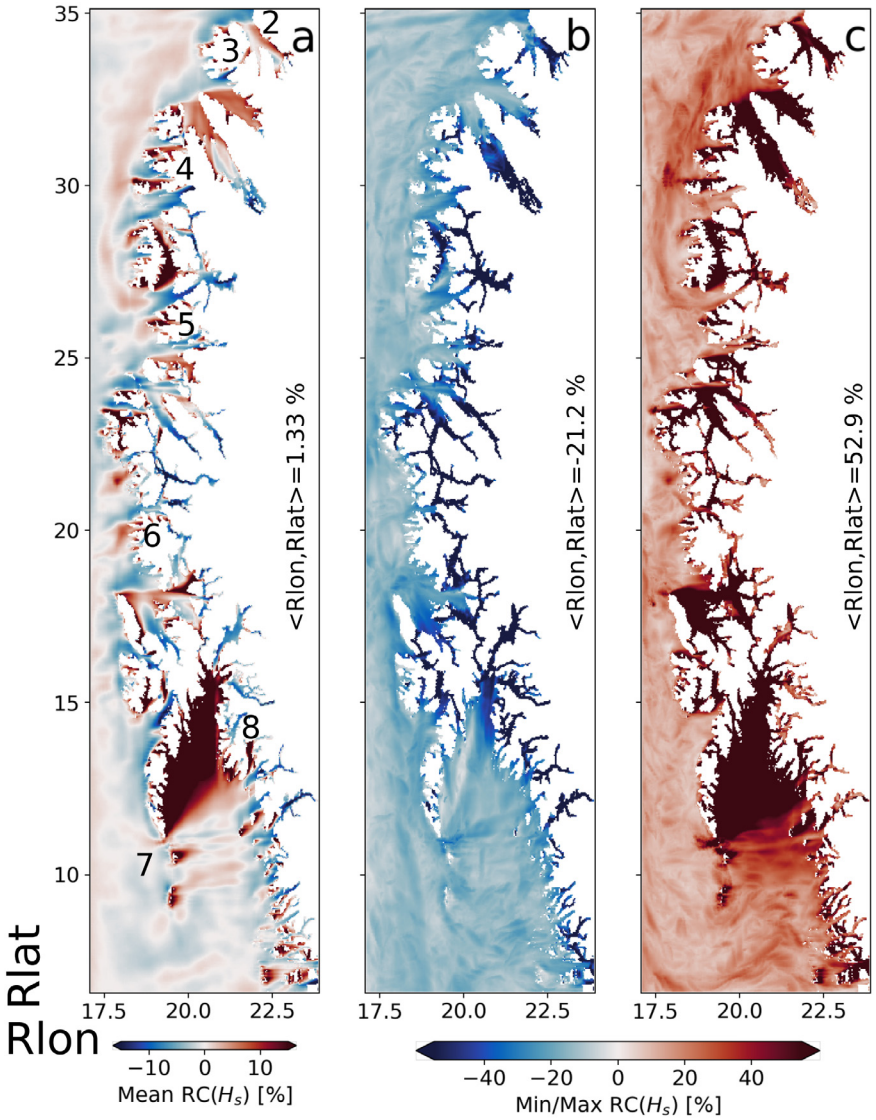

Fig. 8. Horizontal variability of relative change (RC) including the mean (a), and minimum/maximum values [(b)/(c)], computed for the entire study period.

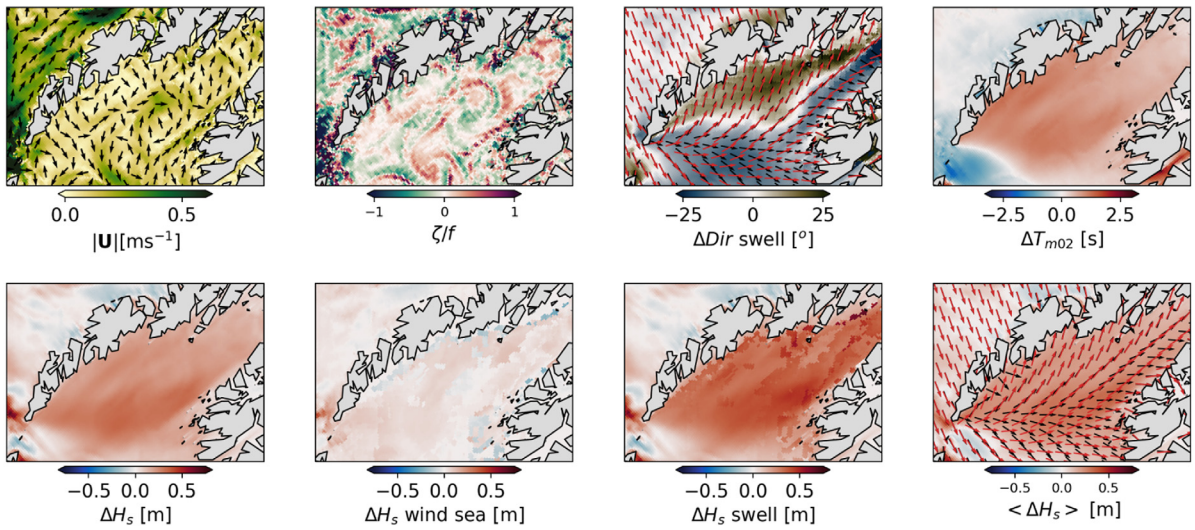

Fig. 9. Advection and current-induced refraction of wave energy in *Vestfjorden* at 2019-01-05T15:00 UTC. Upper panels from left denote the current speed, the vertical vorticity normalized by inertial frequency f, Δ swell direction (black arrows $\mathrm{WAM}_{\mathbf{ref}}$, red arrows $\mathrm{WAM}_{\mathbf{curr}}$), and ΔT_{m02}, respectively. Lower panels from left denote total ΔH_s, the difference for the wind sea, and swell components, and the mean difference for one day centered around 15:00UTC (together with mean swell propagation directions as above), respectively.

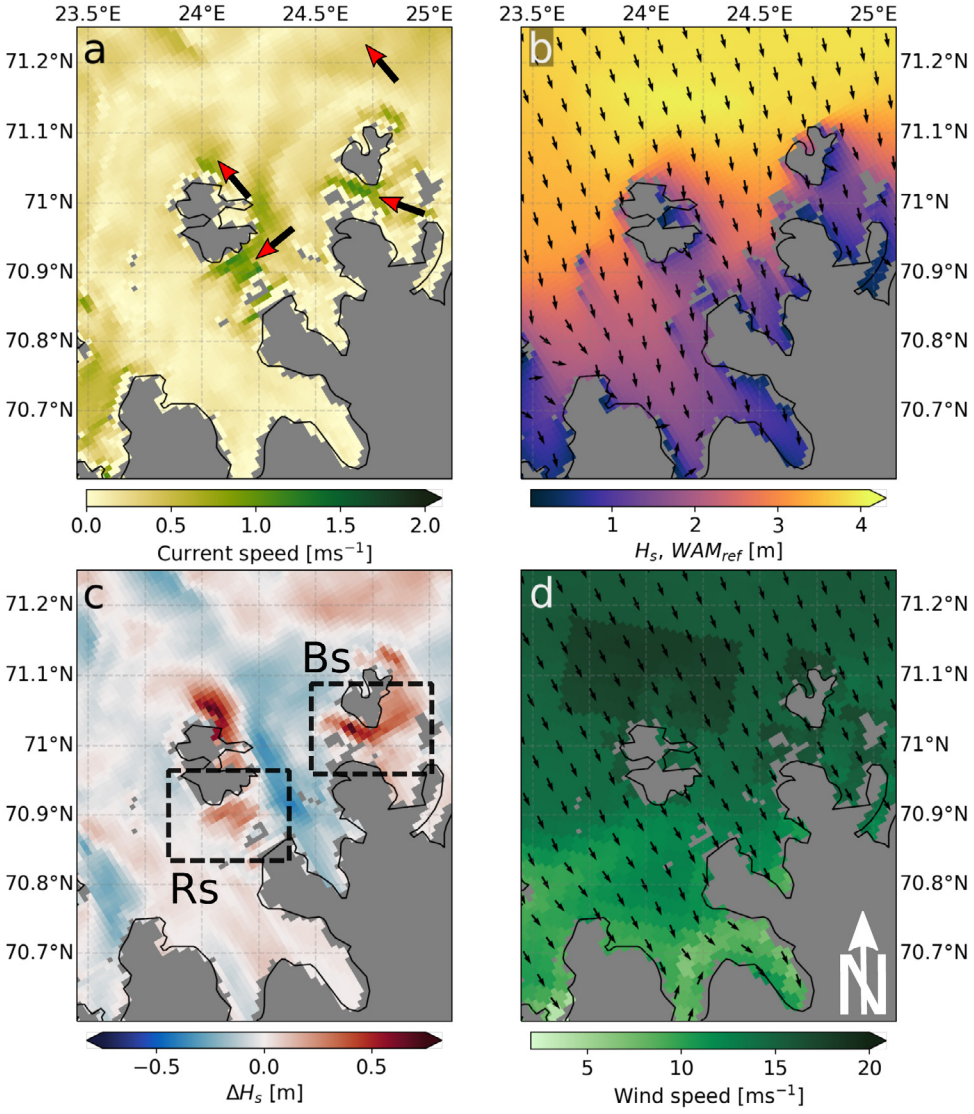

Fig. 10. Model snapshots at 2019-02-21T21 UTC for area 4 (see Fig. 3). Panels show: (a) the ocean current speed overlaid with tidal current direction (red arrows), (b) H_s with overlaid mean wave direction from WAM_{ref}, (c) ΔHs, and (d) wind speed with mean direction (black arrows). Wind, wave, and current conditions are similar to those reported to generate dangerous waves according to Den norske los (2018) in *Rolvsøysundet* (Rs) and *Breisundet* (Bs).

is reported to set up a rough sea state. A model snapshot is shown in Fig. 10. Here, the current meets the waves in Rs and Bs, resulting in an accompanying RC of about 20% and 40%, respectively. Maximum ΔH_s is about 0.7 m in Bs for the entire study period, and maximum RC is about 50%. The location of the areas with increased wave heights are well predicted by WAM_{curr}, together with their associated time scale, as seen in the highlighted rectangle in Fig. 6. The area with the largest positive ΔH_s, north of Rs, is not mentioned in the NPG. One reason could be that it is located on a shallow plateau with depths between 20–70 m, and is thus not used extensively for ship traffic.

3.3.2. Area 5 and 6: Refraction over shallows

Area 5 exhibits mostly positive mean RC over the shallows banks in the area, sometimes exceeding 25% (Figs. 1, 8). Even though the area is reported in NPG, the shallows are not denoted in the nautical charts provided by the Norwegian Mapping Authorities, contrary to all the other areas (https://norgeskart.no/#!?project=norgeskart&layers=1008). Nevertheless, the area is qualitatively resolved in terms of increased wave heights over the shallow regions according to the NPG

The shallow banks outside area 6 are also resolved in WAM_{curr}, with their on average positive RC in H_s up to 15% (Figs. 1, 8a). The shallow banks are also clearly visible in Fig. 6, with temporal modes associated with T_e. According to the NPG, dangerous waves occur when the tidal cycle is in phase with the NCC. The wave heights for northernmost shallow bank outside area 6 increase up to 40% (Fig. 8c). In order to quantify the impact of refraction, we conducted a wave ray-tracing analysis as shown in Fig. 11. Here we have implemented a wave ray-tracing solver for the Cartesian version of Eqs (2)–(5) to qualitatively assess the importance of refraction. Switching off the ambient current, the wave rays for a 14 s period swell converge over the shallow ridge due to depth-induced refraction (Fig. 11d). However, when currents are included, additional wave rays converge over the shallow due to current-induced refraction, causing the increase in H_s in WAM_{curr} (Fig. 11c). Thus, the ambient current acts as a wave guide towards the shallower regions by which the waves becomes trapped by the bathymetry, which in turn yield increasing wave heights.

3.3.3. Area 7: Moskstraumen

Intense wave–current interaction due to *Moskstraumen* occur on both sides of the southern tip of *Lofoten* (location 7– Fig. 1). The west side is known for the maximum H_s modulation, but the in situ observations were collected on the east side (B, Fig. 1). Here, the observed

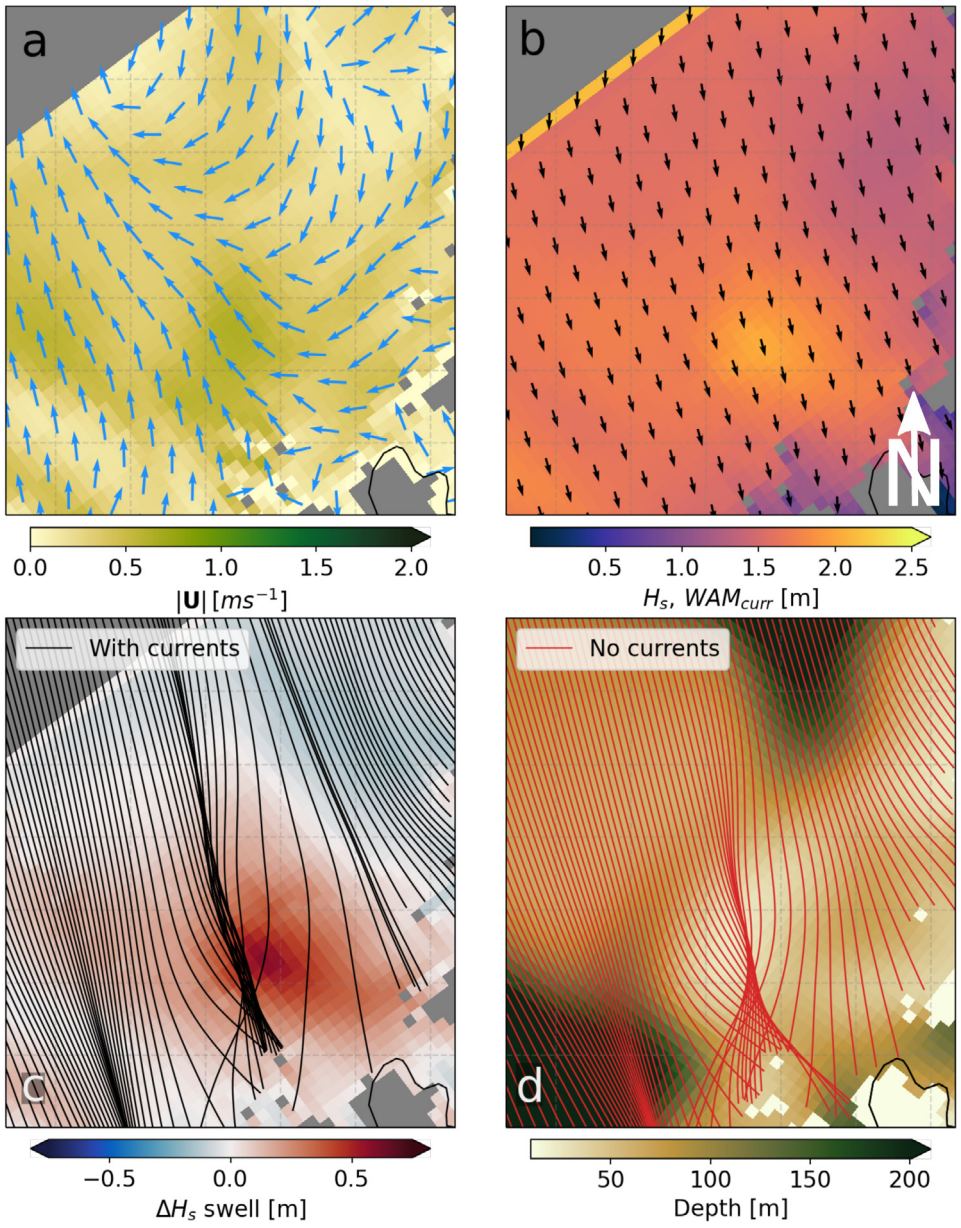

Fig. 11. The impact of current-induced refraction for the northernmost shallow bank in area 6 (see Fig. 3). A $T = 14\ s$ period wave is propagating against the current (panel a) according to the modeled mean swell direction (panel b) using a wave tracing solver. Panels (c) and (d) show the impact of current induced refraction (overlaid swell ΔH_s) and refraction due to bathymetry only (overlaid the depth profile), respectively.

interactions are presented first, followed by a detailed analysis on the west side.

The time series of H_s and the associated wave spectrum during an 8-day spring tide period in January 2019 are shown in Fig. 12. At the end of the period, $\text{WAM}_{\textbf{curr}}$ H_s compares well with the observations at tidal cycles (see black triangles in Figs. 12a,g). Beginning on 23 January, the mean wave propagation direction gradually shifts from west to east following a shift in wind direction (Figs. 12c and d). Thus, wind waves and currents are coming into opposition as the current reaches its maximum. This leads to an increase in energy for the wind sea part of the observed and the $\text{WAM}_{\textbf{curr}}$ spectrum (Figs. 12f,g). A current of 2 m s^{-1} (Fig. 12b) will block opposing wind waves with periods $T = 5$ s and shorter, which correspond well with the observed and modeled wind wave periods of around 0.2 Hz (Figs. 12f,g).

The modeled current maximum is more or less in phase with the observations (Fig. 12b). However, the peak after current maximum is at times out of phase (see black arrows Fig. 12b). Here, the northernmost part of the tidal current that has turned, as it turns westward before the rest of the tidal current (not shown). The turning induces a local horizontal shear of opposing surface currents, known locally as *Strinna*, which gives rise to a complicated sea state (Den norske los, 2018). Thus, for the first highlighted H_s peak, $\text{WAM}_{\textbf{curr}}$ is out of phase with the observations as the eastward (not shown) propagating swell undergo an increase in wave energy due to *Strinna* (see lowest frequencies about 01-23T12:00 UTC Fig. 12f). Nevertheless, the 1D spectrum also reveal enhanced wave energy for the wind sea at current maximum, which corresponds well with the observations (Figs. 12f,g). However, at current maximum, the energy of the aforementioned swell decreases due to following waves and currents leading the decrease in H_s. In the context of numerical ocean modeling, a local phenomenon like *Strinna* can contaminate neighboring grid points due to limited horizontal resolution. This can in turn lead to a mismatch between wave predictions and observations, like in the case just described above. This highlights the challenges of comparing individual model grid points with observations.

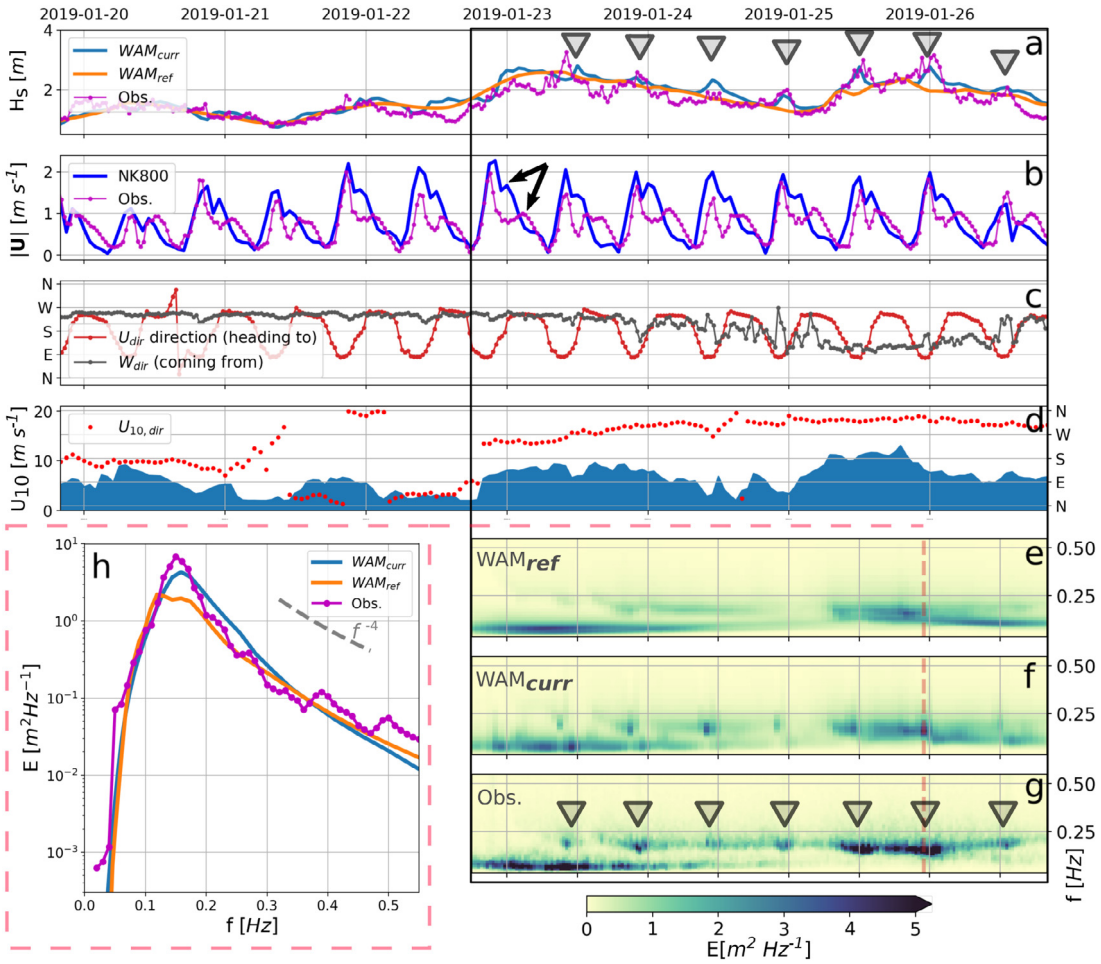

Fig. 12. Time series of modeled and measured wave, current, and wind conditions in *Moskstraumen* during spring tide in January 2019. Panels show: (a) H_s from WAM_{curr} (blue), WAM_{ref} (orange) and ADCP (magenta). Triangles denote when H_s is modulated due to the tidal current heading eastward during a rising tide. (b) modeled (blue) and observed (magenta) current speed (|**U**|). (c) Observed current (red) and mean wave propagation (gray) directions. (d) modeled wind speed (blue) and direction (red dots). The 2D wave energy density spectra from WAM_{ref}, WAM_{curr}, and the ADCP observations are given in panels (e), (f), and (g), respectively. (h) denote the 2D spectrum for a single point in time (see red line panels e–g).

Upon inspection of the 1D spectrum during current maxima we see that the wave energy around the peak frequency is two orders of magnitude larger in WAM_{curr} than WAM_{ref}, and correspond better with the observations (see Fig. 12h). However, the energy decay for the higher frequencies are less compared with the observations, suggesting that the wave dissipation parameterization is too conservative in cases like this.

Even though wave growth due to blocking waves seems to be the dominant mechanism, it most likely occurs in combination with the relative wind and the radiation stresses as also reported by Ardhuin et al. (2012), Vincent (1979). The impact of the relative wind is, however, not quantified in WAM_{curr} (Section 2.1.2). Nevertheless, the wind sea modulation at the peak of the tidal cycle corresponds well with the enhanced wave breaking reported by OS21 (see their Fig. 7). From Fig. 12c, it is perhaps not obvious that the waves and currents oppose each other near the current maximum since the observed mean wave direction can change erratically and sometimes record westward propagating waves. As the ADCP is an Eulerian measurement, these spikes around the current maximum are a result of blocked waves which are advected westward by the strong tidal current. Additional selected cases comparing observations with model results in *Moskstraumen* are given in Appendix.

From the twin experiment intercomparison, maximum H_s modulation in *Moskstraumen* occurs on the western side of *Lofoten*, when the tidal current is heading westward during a falling tide (see area 7 in Fig. 7e). A snapshot from 2019-01-24T05 UTC is shown in Fig. 13. Here, eastward propagating swell opposes the tidal current. Using the aforementioned wave ray-tracing method, a $T = 12$ s period wave train was propagated through the domain. This wave period is representative of the peak period in WAM_{curr} (not shown). We find the focusing of wave ray paths to agree with ΔH_s in the current branch (right panel Fig. 13). Local wind sea is also present, but the swell part of the spectrum is more strongly modulated by the tidal current (not shown). Trapped waves due to tidal currents were also reported by Ardhuin et al. (2012) from their field and model study in the Fromveur passage. In our case, however, the horizontal extent of the tidal current is not sufficiently long for the swell to be reflected back to the center from the edges of the current branch.

The largest ΔH_s west in *Moskstraumen* was about 90%. During periods of relatively calm winds, with H_s between 2–3 m, ΔH_s was about 1.5 m (not shown), giving a relative difference of about 50%. This implies that the current can modify the wave field to the same extent as that of the wind field variations. We also found minimum $\Delta T_{m02} < -3$ s in *Moskstraumen*, which is caused by the increase in wave frequency due to the Doppler shift (Eq. (7)).

4. Discussion

In *Moskstraumen*, the observed temporal scales of wave field modulations are resolved in WAM_{curr} (Figs. 4, 6). The wave energy density

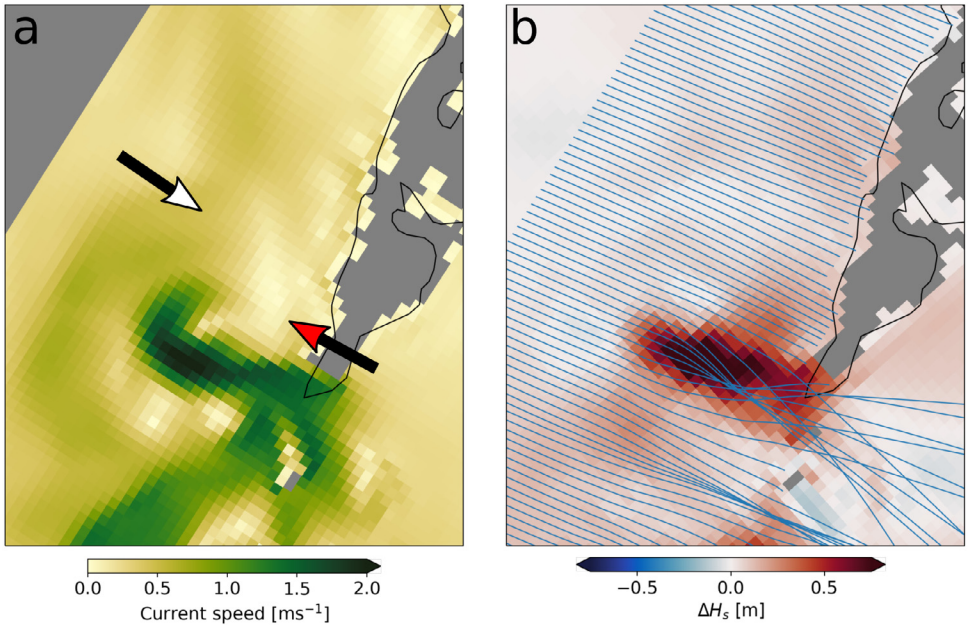

Fig. 13. Model snapshots (2019-01-24T05 UTC) during a falling tide in *Moskstraumen* (area 7 Fig. 3), when the tidal current is heading west. Panel (a) shows the current speed and direction (red arrow) and the dominant swell propagation direction (white arrow). Panel (b) show ΔHs with overlaid wave rays (blue) corresponding to eastward propagating swell with $T = 12$ s from a wave ray tracing solver.

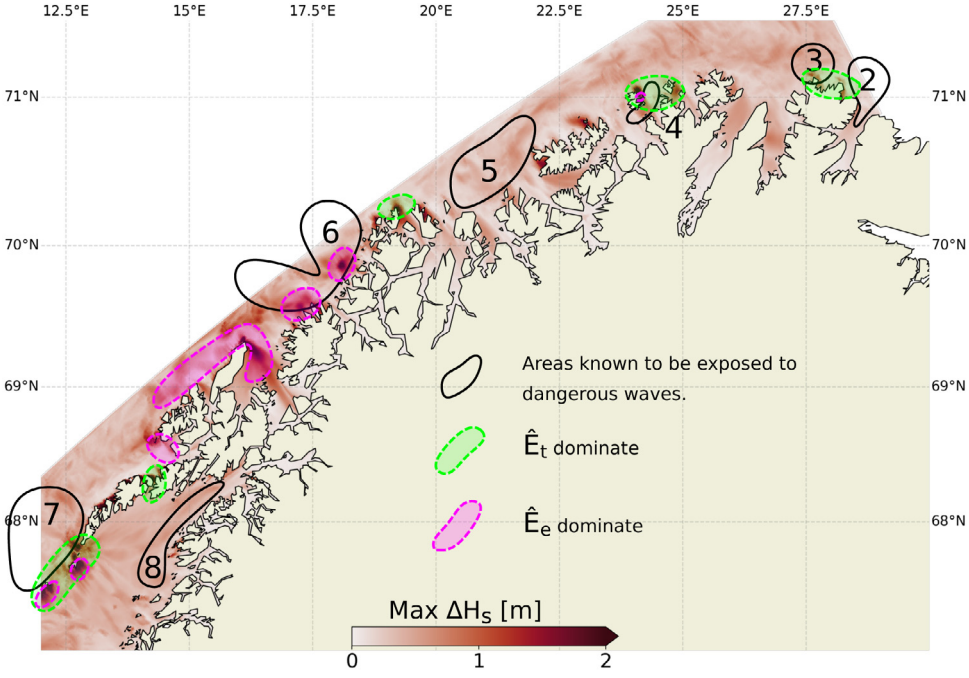

Fig. 14. Maximum ΔH_s for the entire study period (see Fig. 7e) overlaid with the areas known to be exposed to dangerous waves (black solid lines from Fig. 3) together with selected areas with strong temporal H_s variability at different temporal modes (see Fig. 6).

spectrum and the associated H_s are at times also correctly represented by WAM_{curr}, contrary to WAM_{ref} (see Fig. 12). This is in agreement with Ardhuin et al. (2012), who also found their wave model capable of representing the current-induced effects using the same wave dissipation parameterization as in our study. Furthermore, and as shown explicitly in Appendix, the current forcing can impact the wave field to a similar degree to that of wind field, and also provide a more realistic representation of H_s during strong storms (U_{10} = 35 m s^{-1}, ΔH_s ~ 2 m, see Fig. 15d). We find that the largest wave height modulations in tidal currents occur when waves oppose the current. For wind sea, the increase in wave heights are due to wave blocking and energy bunching due to the Doppler shift, whereas refraction is most important for swell. This is also in agreement with previous work (e.g. Baschek, 2005; Ardhuin et al., 2012; Masson, 1996; Romero et al., 2017, 2020). However, deviations between observations and model results suggest that some wave–current interactions are not properly

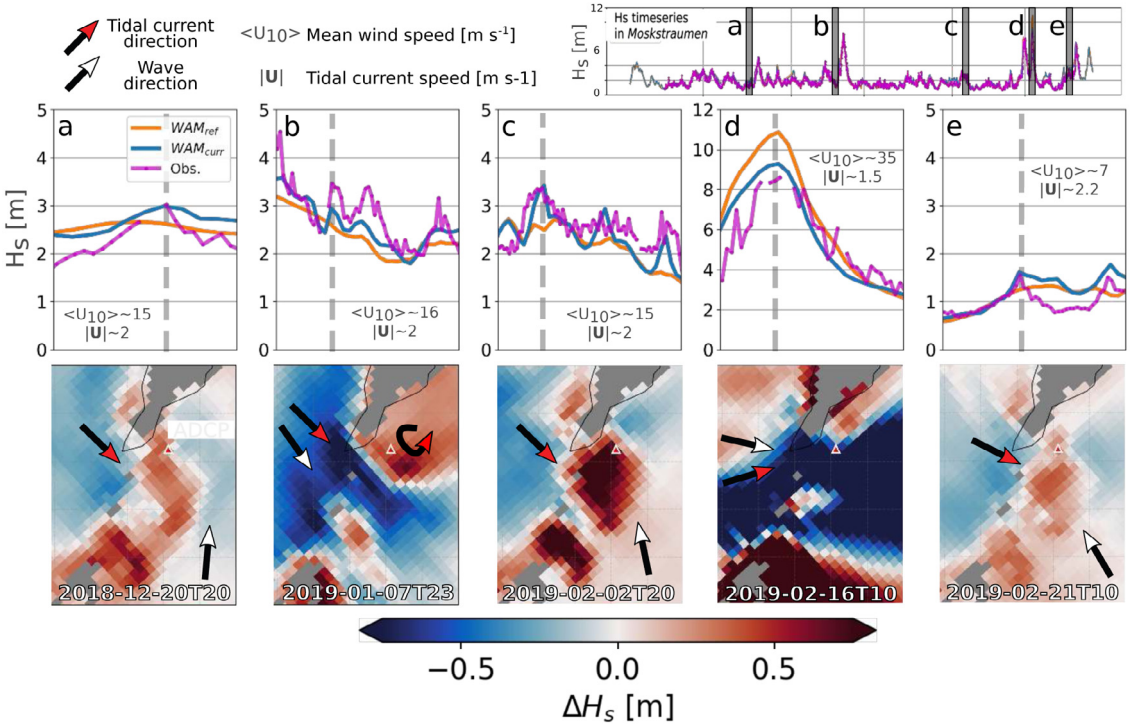

Fig. 15. Comparing H_s representation for selected segments in *Moskstraumen*. Columnwise, panels a-e show a zoomed view on H_s time series for a particular period, with a 2D ΔH_s snapshot associated with the vertical gray line. Arrows filled with red and white represent the tidal current direction and mean wave propagation direction, respectively. The approximate mean wind speed, $\langle U_{10} \rangle$, and maximum current speed, |**U**|, for each of the snapshots are denoted in each time series panel. Red triangle denotes the location of the ADCP.

resolved by the wave model, which is expected due to the limitations of linear theory (Babanin et al., 2017). It is also a reminder of the inaccuracy of comparing single model grid cells with observations.

As the tidal cycles are well resolved WAM_{curr} (Fig. 12f), we consider it valid to extrapolate our analysis from *Moskstraumen* to other areas exposed to tidal currents, despite the lack of observations. This is of particular interest for dangerous wave areas (Fig. 3), and includes area 3, area 4 (Fig. 10), and the west side of *Moskstraumen* (Fig. 13) where we have no in situ measurements. For the latter, the model inter-comparison reveals an increase in H_s of up to 90% in the study period.

On longer time scales, WAM_{curr} qualitatively resolves areas 5 and 6 in the mean (Fig. 7a), but also for single cases (Fig. 11). We find the ambient current to act as a wave guide such that additional wave trains gets trapped by the local bathymetry, ultimately leading to increasing wave heights. The wave and current conditions correspond to what is reported in the NPG (Den norske los, 2018).

We find the proposed method of mapping the spatio-temporal variability differences between two runs in a twin experiment to be useful in identifying regions with intense wave–current interaction (Fig. 6). The information thus provided complements that from the maps of σ and RMSE (see Figs. 7b,c) by clearly distinguishing the dominant spectral regimes at work. When overlaying the most dominant areas in Fig. 6 with the maximum ΔH_s (Fig. 7e) together with the dangerous waves areas (Fig. 3), we see that those that are exposed to strong tidal currents stand out (Fig. 14). As all of these areas were characterized independently in the NPG, i.e. the areas 2–8, we conclude that this demonstrates the importance of including current forcing in high-resolution wave models in areas with strong currents. Their use is two-fold. First, the sort of twin-model runs shown here can be used to identify areas where the sea state is influenced by strong currents, and associated gradients. This can best be done by running twin-model hindcasts over sufficiently long periods and then analyze the difference fields of the two runs using the methodology presented here. In particular, mapping the average (Fig. 7) and maximum (Fig. 14) differences in significant wave height, ΔH_s, and assessing the associated spectral distribution through RGB composites (Fig. 6) are efficient ways to identify such potentially dangerous regions. Secondly, the same method can be employed for real-time forecasting, as is done operationally at the Norwegian Meteorological Institute. By providing maps of the wave height difference from such twin-model forecasts, it is immediately evident when and where situations with strong wave–current interaction can be expected.

In area 8 in *Vestfjorden*, we do not find spiky values in ΔH_s indicating large waves. However, we do find that WAM_{curr} reduces the bias and NRMSE in H_s against altimeter observations (P5 Table 2 and Figs. 5, 7, and 8). For the remainder of the domain, wave height variations mostly occur on shorter horizontal scales than the *Vestfjorden* basin (like P1-P4 in Fig. 5) such that the coarse resolution of Level-3 altimeter observations (about 7 km) is insufficient to reveal the differences. Utilizing Level-2 observations using novel filtering methods, such as Bohlinger et al. (2019) for characterizing wave height variability will be the focus of future studies.

An area that stands out with strong wave field modulation, which is not reported in the NPG, is located between area 6 and 7 in Fig. 3. Our findings show that $\hat{E}_t < \hat{E}_e$ (Fig. 14). However, $\hat{E}(\text{M}_1)$ is in the northernmost part similar to that in *Moskstraumen* (see line *i* Fig. 6). Further south, the wave field modulation occur on frequencies below M_1, suggesting that refraction due to eddies and whirls dominate. More field work experiments is needed to properly assess wave–current interaction in this area.

A limitation in the present study is the use of surface currents and not taking into account the vertical shear of the currents. Even though this can be considered a second order effect, it is expected to have an impact on the wave field (Quinn et al., 2017). On the other hand, tidal currents are often barotropic (like *Moskstraumen* see Fig. 7 in OS21), which justifies the use of surface currents in these areas.

To summarize, five out of seven areas known for dangerous waves are qualitatively resolved in WAM_{curr} in terms of increased wave heights (i.e. 3–7 Fig. 14). For these areas, the dominating cause leading to wave growth agrees with the reports in the NPG. The two remaining areas, i.e. 2 and 8, WAM_{curr} does neither indicate situations with particularly large waves in our study period, nor does it imply large, local horizontal wave height gradients. Nevertheless, the large mean relative H_s increase in *Vestfjorden* together with the bias reduction against altimeter observations show that the wave field representation in this region is improved in WAM_{curr}.

Based on the results and the discussion above we argue that current forcing should be included in wave forecasts in our study region. In particular tidal currents as they enforce the largest wave field variability and makes a large impact on the wave heights. Spectral wave models have for decades proven to yield good predictions of the sea state, including under extreme storm events (Aarnes et al., 2012). However, with the advent of high-resolution operational ocean models capable of faithfully resolving the tidal and baroclinic current field, the modulation of the wave field by spatially varying currents should also be taken into account.

5. Conclusion

In a twin wave model study in Northern Norway we have investigated the impact of current forcing in spectral wave models. This is an area exposed to waves from the open ocean, and an ocean circulation which is dominated by tides and energetic currents with associated eddies. We find the wave model with current forcing to qualitatively resolve several areas that are reported in the Norwegian Pilot Guide for their large, and sometimes dangerous, waves due to intense wave–current interaction. This is in contrast to the wave model without current forcing. The dominating physical mechanism leading to increased wave heights also correspond to the reports in the Pilot Guide. Further to this, our results indicate that some areas undergo strong wave height modulations, which are not reported in the Pilot Guide.

We find the proposed diagnostic method for mapping temporal variability in twin model experiments to be convenient in analyzing regions dominated by ocean dynamics on different time scales. It is easy to implement and simple to adjust in terms of frequency ranges of interest. In this work we focused mainly on the modulation of the significant wave height.

Tidal currents induce the largest absolute wave height discrepancies between the two model runs. We find the magnitude and phase in wave height variability to be well represented in *Moskstraumen*, which is one of the world's strongest tidal currents in the open ocean. Here, we find wave height deviations between the twin model runs up to 50% to corroborate with observations. Furthermore, and in absence of direct observations, we find inter model H_s differences up to 90% in tidal currents.

Maximum relative wave height discrepancies were found in areas sheltered from the open ocean and with less energetic currents, like *Vestfjorden*. Here, we find a better correspondence between altimeter observations of H_s and the wave model predictions with current forcing. Refraction and advection of wave action reduces the bias and RMSE by up to 16% and 18%, respectively, for specific periods. The spatial extent of *Vestfjorden* is also large enough to be sufficiently resolved by conventional Level-3 altimeter observations.

Inclusion of current forcing is still uncommon at operational centers (Palmer and Saulter, 2016; Staneva et al., 2015; Kanarik et al., 2021; Rapizo et al., 2018). We would suggest to include current forcing in the wave forecast models covering Northern Norway. Particularly in areas with strong tidal currents, the current forcing enforce an improved representation of the wave field for the end users.

CRediT authorship contribution statement

Trygve Halsne: Conceptualization, Methodology, Investigation, Writing – original draft. **Patrik Bohlinger:** Validation, Writing – original draft. **Kai Håkon Christensen:** Writing – original draft, Supervision. **Ana Carrasco:** Resources. **Øyvind Breivik:** Writing – original draft, Supervision.

Declaration of competing interest

The authors declare that they have no known competing financial interests or personal relationships that could have appeared to influence the work reported in this paper.

Acknowledgments

This research was partly funded by the Research Council of Norway through the project MATNOC, Grant No 308796. We greatly appreciate all the help from employees at Nortek AS and the Norwegian Coastal Administration who made possible the instrument deployment as well as acquiring, processing, and analyzing the ADCP data. ØB gratefully acknowledges the support by the Research Council of Norway through the Stormrisk project (Grant No 300608). TH would like to thank Thomas Lavergne for fruitful discussions concerning data visualization.

Appendix. Additional selected cases in Moskstraumen

Five additional segments to Section 3.3.3 concerning the impact of *Moskstraumen* on the wave field are presented in Fig. 15. All during rising tide, i.e. with an eastward oriented current. In Fig. 15a, H_s increases as wind waves meet an opposing current. Prior to this model snapshot, the H_s observations are invalid due to the tilt of the ADCP, here indicated by the missing line in the time series panel. Nevertheless, as the current speed starts decreasing, there is a good agreement between the observations and H_s predicted by WAM_{curr} during maximum current speed. Otherwise, WAM_{ref} is actually closer. There are, however, large horizontal gradients in ΔH_s as is evident from the two-dimensional (2D) views (lower panels in Fig. 15). Thus, comparing instead with neighboring grid points yielded slightly different results, except near the peak (not shown). Similarly, the event in Fig. 15c is also exposed to opposing wind waves and currents. The first and last peak in H_s are resolved by WAM_{curr} but not by WAM_{ref}.

For the event in Fig. 15b, both wave model runs predict a strong, large-scale gradient in H_s between the west (5 m) and east side (2 m) of the *Moskens Sound* (not shown). There is also a shear in the ocean current between the tidal current heading eastward, and a current following the coast west off *Lofotodden*, ending in a clockwise rotating eddy. The area sees frequent generation of eddies and dipoles due to the tidal current (see Fig. 9 OS21 and Fig. 8 Børve et al., 2021). The positive Doppler shift due to the wave-following tidal current stretches the waves and increases the wave period, with an accompanied decrease in wave amplitude in WAM_{curr}. Waves are also advected both by the tidal current and the NCC, giving rise to a region where wave action density accumulates. In addition, when escaping the tidal current, the waves experience a negative Doppler shift and thus an increase energy, as also reported by Romero et al. (2017).

The most extreme wave conditions in the study period occurred in late February, with H_s modeled to be around 9 m and 11 m by WAM_{curr} and WAM_{ref}, respectively (Fig. 15d). The observations were just below 8.5 m. The tidal current, although weaker than in the other cases, was oriented in the same overall direction as the waves, giving a strong reduction in H_s within the branch of the tidal current (negative ΔH_s region in Fig. 15d). There is an increase in H_s towards the coast, most likely due to refraction since the current speed is weaker towards the coast (Palmer and Saulter, 2016).

For the last event, the current exceeded 2 m s^{-1} and the wind speed was below 10 m s^{-1} heading north-west (Fig. 15e). Between the two

tidal cycles, both wave models over-predict H_s, but only $\mathrm{WAM}_{\mathbf{curr}}$ resolved the wave height modulations. This example demonstrates that the tidal current can impact the wave field to a similar degree to that of the wind field, with variations in H_s of the order of 50%. The second peak in Fig. 15e covered the maximum relative change in our measurement period, which was 55.6% (at 2019-02-21T22 UTC).

References

Aarnes, O.J., Breivik, O., Reistad, M., 2012. Wave extremes in the northeast atlantic. J. Clim. 25 (5), 1529–1543. http://dx.doi.org/10.1175/JCLI-D-11-00132.1, Publisher: American Meteorological Society Section: Journal of Climate, URL: https://journals.ametsoc.org/view/journals/clim/25/5/jcli-d-11-00132.1.xml.

Albretsen, J., Sperrevik, A.K., Staalstrøm, A., Sandvik, A.D., Vikebø, F., Asplin, L., 2011. NorKyst-800 Report No. 1: User Manual and Technical Descriptions, Tech. Rep. 2. Technical Report, Institute of Marine Research, Bergen, Norway, URL: https://www.hi.no/en/hi/nettrapporter/fisken-og-havet/2011/fh_2-2011_til_web.

Ardhuin, F., Gille, S.T., Menemenlis, D., Rocha, C.B., Rascle, N., Chapron, B., Gula, J., Molemaker, J., 2017. Small-scale open ocean currents have large effects on wind wave heights. J. Geophys. Res. Oceans 122 (6), 4500–4517. http://dx.doi.org/10.1002/2016JC012413, _eprint: https://agupubs.onlinelibrary.wiley.com/doi/pdf/10.1002/2016JC012413, URL: https://agupubs.onlinelibrary.wiley.com/doi/abs/10.1002/2016JC012413.

Ardhuin, F., Rogers, E., Babanin, A.V., Filipot, J.-F., Magne, R., Roland, A., Westhuysen, A.v.d., Queffeulou, P., Lefevre, J.-M., Aouf, L., Collard, F., 2010. Semiempirical dissipation source functions for ocean waves. part I: Definition, calibration, and validation. J. Phys. Oceanogr. 40 (9), 1917–1941. http://dx.doi.org/10.1175/2010JPO4324.1, Publisher: American Meteorological Society Section: Journal of Physical Oceanography, URL: https://journals.ametsoc.org/view/journals/phoc/40/9/2010jpo4324.1.xml.

Ardhuin, F., Roland, A., Dumas, F., Bennis, A.-C., Sentchev, A., Forget, P., Wolf, J., Girard, F., Osuna, P., Benoit, M., 2012. Numerical wave modeling in conditions with strong currents: Dissipation, refraction, and relative wind. J. Phys. Oceanogr. 42 (12), 2101–2120. http://dx.doi.org/10.1175/JPO-D-11-0220.1, _eprint: https://journals.ametsoc.org/jpo/article-pdf/42/12/2101/4520148/jpo-d-11-0220_1.pdf.

Babanin, A.V., Rogers, W., De Camargo, R., Doble, M., Durrant, T., Filchuk, K., Ewans, K., Hemer, M., Janssen, T., Kelly-Gerreyn, B., MacHutchon, K., Mccomb, P., Qiao, F., Schulz, E., Skvortsov, A., Thomson, J., Vichi, M., violante carvalho, N., Wang, D., Young, I., 2019. Waves and swells in high wind and extreme fetches, measurements in the southern ocean. Front. Mar. Sci. 6, 361. http://dx.doi.org/10.3389/fmars.2019.00361.

Babanin, A.V., van der Weshuijsen, A., Chalikov, D., Rogers, W.E., 2017. Advanced wave modeling, including wave-current interaction. J. Mar. Res. 75 (3), 239–262. http://dx.doi.org/10.1357/002224017821836798.

Baschek, B., 2005. Wave–current interaction in tidal fronts. In: Rogue Waves: Proc. 14th 'Aha Huliko'a Hawaiian Winter Workshop. University of Hawaii at Manoa, Honolulu, HI, pp. 131–138.

Behrens, A., Staneva, J., Saetra, Ø., Janssen, P., 2013. Documentation of a Web Based Source Code Library for WAM. Technical Report, Helmholtz-Zentrum Geestacht,Geesthacht, Germany, URL: http://met-xpprod.customer.enonic.io/sokeresultat/_/attachment/inline/c1fdc351-1109-47fc-9d9e-65c9f31eaccb:b52dfe2b5953103564a339bb290b83c66b1315f6/MyWave_Report_D1.1.pdf.

Bohlinger, P., Breivik, Ø., Economou, T., Müller, M., 2019. A novel approach to computing super observations for probabilistic wave model validation. Ocean Model. 139, 101404. http://dx.doi.org/10.1016/j.ocemod.2019.101404, URL: https://www.sciencedirect.com/science/article/pii/S1463500319300435.

Børve, E., Isachsen, P.E., Nøst, O.A., 2021. Rectified tidal transport in Lofoten-Vesterålen, Northern Norway. Ocean Sci. Discuss. 1–33. http://dx.doi.org/10.5194/os-2021-41, Publisher: Copernicus GmbH, URL: https://os.copernicus.org/preprints/os-2021-41/.

Cavaleri, L., Fox-Kemper, B., Hemer, M., 2012. Wind waves in the coupled climate system. Bull. Am. Meteorol. Soc. 93 (11), 1651–1661. http://dx.doi.org/10.1175/BAMS-D-11-00170.1, Publisher: American Meteorological Society Section: Bulletin of the American Meteorological Society. URL: https://journals.ametsoc.org/view/journals/bams/93/11/bams-d-11-00170.1.xml.

Christensen, K.H., Sperrevik, A.K., Broström, G., 2018. On the variability in the onset of the Norwegian coastal current. J. Phys. Oceanogr. 48 (3), 723–738. http://dx.doi.org/10.1175/JPO-D-17-0117.1, Publisher: American Meteorological Society Section: Journal of Physical Oceanography. URL: https://journals.ametsoc.org/view/journals/phoc/48/3/jpo-d-17-0117.1.xml.

Den norske los, 2018. The Norwegian Pilot Guide—Sailing Directions for the Norwegian Coast, Svalbard and Jan Mayen. The Norwegian Mapping Authority, Stavanger, Norway.

Dysthe, K.B., 2001. Refraction of gravity waves by weak current gradients. J. Fluid Mech. 442, 157–159. http://dx.doi.org/10.1017/S0022112001005237, Publisher: Cambridge University Press. URL: https://www.cambridge.org/core/journals/journal-of-fluid-mechanics/article/abs/refraction-of-gravity-waves-by-weak-current-gradients/BCA46BDBE52EDC210719E9CC95DA7ECB.

Gemmrich, J., Garrett, C., 2012. The signature of inertial and tidal currents in offshore wave records. J. Phys. Oceanogr. 42 (6), 1051–1056. http://dx.doi.org/10.1175/JPO-D-12-043.1, Place: Boston MA, USA Publisher: American Meteorological Society. URL: https://journals.ametsoc.org/view/journals/phoc/42/6/jpo-d-12-043.1.xml.

Gjevik, B., Moe, H., Ommundsen, A., 1997. Sources of the melstrom. NAT 388, 837–838. http://dx.doi.org/10.1038/42159.

Hasselmann, S., Hasselmann, K., Allender, J.H., Barnett, T.P., 1985. Computations and parameterizations of the nonlinear energy transfer in a gravity-wave specturm. part II: Parameterizations of the nonlinear energy transfer for application in wave models. J. Phys. Oceanogr. 15 (11), 1378–1391. http://dx.doi.org/10.1175/1520-0485(1985)015<1378:CAPOTN>2.0.CO;2, Publisher: American Meteorological Society Section: Journal of Physical Oceanography. URL: https://journals.ametsoc.org/view/journals/phoc/15/11/1520-0485_1985_015_1378_capotn_2_0_co_2.xml.

Holthuijsen, L.H., 2007. Waves in Oceanic and Coastal Waters. Cambridge University Press, http://dx.doi.org/10.1017/CBO9780511618536.

Kanarik, H., Tuomi, L., Björkqvist, J.-V., Kärnä, T., 2021. Improving baltic sea wave forecasts using modelled surface currents. Ocean Dyn. 71 (6), 635–653. http://dx.doi.org/10.1007/s10236-021-01455-y.

Komen, G.J., Cavaleri, L., Doneland, M., Hasselmann, K., Hasselmann, S., Janssen, P.A.E.M. (Eds.), 1994. Dynamics and Modelling of Ocean Waves. Cambridge Univeristy Press, http://dx.doi.org/10.1017/CBO9780511628955.

Kristensen, N.M., Gusdal, Y., 2021. NorKyst800 Model Currents Validation. MET Report, (2/2021), Norwegian Meteorological Institute, p. 44, URL: https://www.met.no/publikasjoner/met-report/_/attachment/download/8b99ea1b-200f-4a09-9eb7-3ada0580e157:56ff9d6c44186aa495be038a1cc5dd84d3ca3f2a/MET-report-02-2021.pdf.

Marechal, G., Ardhuin, F., 2021. Surface currents and significant wave height gradients: Matching numerical models and high-resolution altimeter wave heights in the agulhas current region. J. Geophys. Res. Oceans 126 (2), http://dx.doi.org/10.1029/2020JC016564, e2020JC016564. _eprint: https://agupubs.onlinelibrary.wiley.com/doi/pdf/10.1029/2020JC016564. URL: https://agupubs.onlinelibrary.wiley.com/doi/abs/10.1029/2020JC016564.

Marin, C., Bovolo, F., Bruzzone, L., 2015. Building change detection in multitemporal very high resolution SAR images. IEEE Trans. Geosci. Remote Sens. 53 (5), 2664–2682. http://dx.doi.org/10.1109/TGRS.2014.2363548, Conference Name: IEEE Transactions on Geoscience and Remote Sensing.

Masson, D., 1996. A case study of wave–current interaction in a strong tidal current. J. Phys. Oceanogr. 26 (3), 359–372. http://dx.doi.org/10.1175/1520-0485(1996)026<0359:ACSOWI>2.0.CO;2, _eprint: https://journals.ametsoc.org/jpo/article-pdf/26/3/359/4424891/1520-0485(1996)026_0359_acsowi_2_0_co_2.pdf.

Mathiesen, M., 1987. Wave refraction by a current whirl. J. Geophys. Res. Oceans 92 (C4), 3905–3912. http://dx.doi.org/10.1029/JC092iC04p03905, _eprint: https://agupubs.onlinelibrary.wiley.com/doi/pdf/10.1029/JC092iC04p03905. URL: https://agupubs.onlinelibrary.wiley.com/doi/abs/10.1029/JC092iC04p03905.

McWilliams, J.C., 2016. Submesoscale currents in the ocean. Proc. R. Soc. A Math. Phys. Eng. Sci. 472 (2189), 20160117. http://dx.doi.org/10.1098/rspa.2016.0117, Publisher: Royal Society. URL: https://royalsocietypublishing.org/doi/10.1098/rspa.2016.0117.

Mork, M., 1981. Circulation phenomena and frontal dynamics of the norwegian coastal current. Philos. Trans. R. Soc. Lond. Ser. A Math. Phys. Sci. 302 (1472), 635–647, Publisher: The Royal Society. URL: https://www.jstor.org/stable/37043.

Müller, M., Batrak, Y., Kristiansen, J., Køltzow, M.A., Noer, G., Korosov, A., 2017. Characteristics of a convective-scale weather forecasting system for the European arctic. Mon. Weather Rev. 145 (12), 4771–4787. http://dx.doi.org/10.1175/MWR-D-17-0194.1, Publisher: American Meteorological Society Section: Monthly Weather Review. URL: https://journals.ametsoc.org/view/journals/mwre/145/12/mwr-d-17-0194.1.xml.

Palmer, T., Saulter, A., 2016. Evaluating the Effects of Ocean Current Fields on a UK Regional Wave Model. Technical Report, (612), UK Met Office, Exeter, United Kingdom, p. 35, URL: https://library.metoffice.gov.uk/Portal/Default/en-GB/RecordView/Index/212801.

Quinn, B.E., Toledo, Y., Shrira, V.I., 2017. Explicit wave action conservation for water waves on vertically sheared flows. Ocean Model. 112, 33–47. http://dx.doi.org/10.1016/j.ocemod.2017.03.003, URL: https://www.sciencedirect.com/science/article/pii/S1463500317300288.

Rapizo, H., Durrant, T.H., Babanin, A.V., 2018. An assessment of the impact of surface currents on wave modeling in the Southern ocean. Ocean Dyn. 68 (8), 939–955. http://dx.doi.org/10.1007/s10236-018-1171-7.

Röhrs, J., Christensen, K.H., 2015. Drift in the uppermost part of the ocean. Geophys. Res. Lett. 42 (23), 10,349–10,356. http://dx.doi.org/10.1002/2015GL066733, _eprint: https://onlinelibrary.wiley.com/doi/pdf/10.1002/2015GL066733. URL: https://onlinelibrary.wiley.com/doi/abs/10.1002/2015GL066733.

Romero, L., Hypolite, D., McWilliams, J.C., 2020. Submesoscale current effects on surface waves. Ocean Model. 153, 101662. http://dx.doi.org/10.1016/j.ocemod.2020.101662, URL: http://www.sciencedirect.com/science/article/pii/S1463500320301645.

Romero, L., Lenain, L., Melville, W.K., 2017. Observations of surface wave–current interaction. J. Phys. Oceanogr. 47 (3), 615–632. http://dx.doi.org/10.1175/JPO-D-16-0108.1, _eprint: https://journals.ametsoc.org/jpo/article-pdf/47/3/615/4587128/jpo-d-16-0108_1.pdf.

Saetra, Ø., Halsne, T., Carrasco, A., Breivik, Ø., Pedersen, T., Christensen, K.H., 2021. Intense interactions between ocean waves and currents observed in the lofoten maelstrom. J. Phys. Oceanogr. -1 (aop), http://dx.doi.org/10.1175/JPO-D-20-0290.1, Publisher: American Meteorological Society Section: Journal of Physical Oceanography. URL: https://journals.ametsoc.org/view/journals/phoc/aop/JPO-D-20-0290.1/JPO-D-20-0290.1.xml.

Segtnan, O.H., 2014. Wave refraction analyses at the coast of Norway for offshore applications. Energy Procedia 53, 193–201. http://dx.doi.org/10.1016/j.egypro.2014.07.228, URL: https://linkinghub.elsevier.com/retrieve/pii/S1876610214011059.

Shchepetkin, A.F., McWilliams, J.C., 2005. The regional oceanic modeling system (ROMS): A split-explicit, free-surface, topography-following-coordinate oceanic model. JPO 9, 347–404. http://dx.doi.org/10.1016/j.ocemod.2004.08.002.

Staneva, J., Behrens, A., Wahle, K., 2015. Wave modelling for the German Bight coastal-ocean predicting system. J. Phys. Conf. Ser. 633, 012117. http://dx.doi.org/10.1088/1742-6596/633/1/012117, Publisher: IOP Publishing.

Vincent, C.E., 1979. The interaction of wind-generated sea waves with tidal currents. J. Phys. Oceanogr. 9 (4), 748–755. http://dx.doi.org/10.1175/1520-0485(1979)009<0748:TIOWGS>2.0.CO;2, Place: Boston MA, USA Publisher: American Meteorological Society. URL: https://journals.ametsoc.org/view/journals/phoc/9/4/1520-0485_1979_009_0748_tiowgs_2_0_co_2.xml.